AFRL-OSR-VA-TR-2014-0263

Propagation and Interactions of Ultrahigh Power Light

Donald Umstadter
UNIVERSITY OF NEBRSKA

10/02/2014
Final Report

Air Force Research Laboratory
AF Office Of Scientific Research (AFOSR)/ RTB
Arlington, Virginia 22203
Air Force Materiel Command

REPORT DOCUMENTATION PAGE

Form Approved
OMB No. 0704-0188

1. REPORT DATE *(DD-MM-YYYY)*	**2. REPORT TYPE**	**3. DATES COVERED** *(From - To)*
09-30-2014	Final Technical	7/1/11 - 6/30/14

4. TITLE AND SUBTITLE

Propagation and Interactions of Ultrahigh Power Light: Relativistic Nonlinear Optics

5a. CONTRACT NUMBER

5b. GRANT NUMBER
FA9550-11-1-0157

5c. PROGRAM ELEMENT NUMBER

6. AUTHOR(S)

Donald Umstadter; Sudeep Banerjee; Bradley Shadwick; Serguei Kalmykov

5d. PROJECT NUMBER

5e. TASK NUMBER

5f. WORK UNIT NUMBER

7. PERFORMING ORGANIZATION NAME(S) AND ADDRESS(ES)

University of Nebraska- Lincoln
Office of Sponsored Programs
301 Canfield, PO Box 880433
Lincoln, NE 68588-0433

8. PERFORMING ORGANIZATION REPORT NUMBER

25-0521-0158-001 Final

9. SPONSORING / MONITORING AGENCY NAME(S) AND ADDRESS(ES)

Air Force Office of Scientific Research
Suite 325, Room 3112
875 Randolph Street
Arlington, VA 22203-1768

10. SPONSOR/MONITOR'S ACRONYM(S)

AFOSR

11. SPONSOR/MONITOR'S REPORT NUMBER(S)

12. DISTRIBUTION / AVAILABILITY STATEMENT

Distribution A-Approved for public release

13. SUPPLEMENTARY NOTES

14. ABSTRACT

We present the results of our research on the study of the propagation and interaction of ultrahigh-power light. We implemented new techniques to characterize, control, and optimize the spectral and spatial characteristics of a high-power laser leading to diffraction-limited and transform-limited pulses on target. We simultaneously optimized the on-target characteristics of two pulses at different wavelengths (800 and 400 nm). These improvements resulted in breakthrough scientific applications. We demonstrated tunable laser-driven wakefield acceleration of electron beams with minimal dark current. A novel electron accelerator with separate injection and acceleration stages was developed. It produces electron beams with high charge to ensure the electron beam parameters (charge, energy spread, and divergence) remain constant as the central energy is tuned over 50-300 MeV. Another significant achievement was the development of a tunable (50 keV – 10 MeV), narrowband x-ray source with brightness 3 to 4 orders of magnitude higher than conventional sources. Detailed numerical simulations were performed to understand the physics of these processes. The advances described in this report lend themselves to our planned research in nonlinear Compton scattering and rad

15. SUBJECT TERMS

Controllable laser pulse, high-brightness x-ray beams, tunable electron accelerator, numerical simulations

16. SECURITY CLASSIFICATION OF:			**17. LIMITATION OF ABSTRACT**	**18. NUMBER OF PAGES**	**19a. NAME OF RESPONSIBLE PERSON**
a. REPORT	**b. ABSTRACT**	**c. THIS PAGE**	unclassified	29	**19b. TELEPHONE NUMBER** *(include area code)*
unclassified	unclassified	unclassified			

University of Nebraska

Final Report

Propagation and Interactions of Ultrahigh Power Light: Relativistic Nonlinear Optics

Contract/Grant #: FA9550-11-1-0157

Donald Umstadter (PI)
Bradley Shadwick
Sudeep Banerjee
Serguei Kalmykov

September 30, 2014

Contents

Executive Summary

In this report, we present the results of our work during the three-year project on the study of the propagation and interaction of ultrahigh-power light. This study encompassed several distinct areas with the goal of advancing the understanding of the physics underlying the interaction of ultrashort, high-intensity laser light, with free electrons, atoms and plasmas. The fundamental research has led to several important applications, such as femtosecond-duration electron and hard x-ray sources. This work was performed using the DIOCLES laser system (100-TW and 1-PW beamlines) at the University of Nebraska-Lincoln (UNL), whose development was funded by prior AFOSR support. The advances described in this report will be applied to the next phase of research where we will investigate electrodynamical phenomena in the regime where nonlinear effects such as radiation damping become significant.

In order to study the propagation and interaction of ultrahigh-power light, we implemented new techniques to characterize and optimize high-power laser pulses in spatial and spectral domains. As a result of these breakthroughs, we demonstrated that we could achieve diffraction-limited and transform-limited pulses on target. Moreover, the implementation of feedback loops for both the spatial and time domains enabled us to tailor the pulse characteristics. With this improvement, we could precisely control the evolution of these pulses in underdense media. This proved to be of crucial importance for optimizing the performance of electron accelerators and x-ray sources. Recently, we were able to simultaneously optimize the focusing of both the fundamental and second harmonic which will enable implementation of novel two-color experiments at relativistic intensities, such as field-ionization and injection of electrons into laser wakefields.

Using controllable high-power laser pulses, we demonstrated that laser-wakefield electron accelerators based on the self-injection process could be optimized to produce a tunable, high-brightness electron beam with negligible dark current. Mixed-gas targets allowed us to overcome the low charge of this system. While prior studies in this area showed polychromatic beams that were unstable, we implemented a novel dual-jet target that enabled stable operation over a broad range. By having separate injection and acceleration stages, we could increase the beam charge and ensure that the electron beam parameters, such as charge, energy spread and divergence, remained constant as the central energy was tuned.

This state-of-the-art electron accelerator was used to develop a multi-MeV x-ray source based on Thomson scattering. In this process, two laser pulses are used—the first drives the electron accelerator and the second scatters off the electron beam—to produce a forward directed beam of x-rays. This result represents a breakthrough in the development of table-top x-ray sources. For the first time, we have demonstrated a tunable (50 keV – 10 MeV), narrowband x-ray source with brightness 3 to 4 orders of magnitude higher than conventional sources. The spectral tunability makes possible applications ranging from medical imaging to nuclear photodisintegration.

We also studied some of the basic physics associated with this regime of interaction, such as the roles of spectral and spatial evolution on pulse propagation. Detailed numerical simulations were performed in support of experimental results to explore the physics of this unique regime. The x-ray source has been used for preliminary experiments in high-resolution radiography. The results of this work were presented as invited talks at numerous conferences and were published in the highest impact journals, such as *Nature Photonics* and *Physical Review Letters*.

1. Controllable laser pulses from the high-power Diocles laser system

The experimental work reported here was performed using the high-power Diocles laser system that consists of two beam lines (100-TW and 1 PW) with repetition rate of 10 Hz and 0.1 Hz respectively[1] . The 100-TW system was built in collaboration with THALES LASER. It is a CPA laser system [2], seeded by an ultra-short broadband nano-joule oscillator (SYNERGY, FEMTOLASERS, Inc.) at 76 MHz with pulse duration of 12 fs. An acoustic-optical programmable dispersion filter (AOPDF) (DAZZLER, FASTLITE, Inc.) is installed before the stretcher. The AOPDF is used to modify the spectrum of the seed pulse into the amplifier in order to minimize the gain narrowing effect, as well as compensate residual chromatic dispersion. The repetition rate of the pulses is stepped down to 1 kHz by the AOPDF. An Offner-type stretcher expands the femtosecond pulse to 500 ps in order to avoid nonlinear effects and damage especially in the final amplification stages for petawatt beamline. The stretched pulse is then amplified to 1.3 mJ in a 1 kHz nine-pass amplifier (FEMTOPOWER, FEMTOLASERS, Inc.) pumped by a 9 mJ intra-cavity frequency doubled Nd:YLF laser (JADE, THALES LASER). An electro-optic pulse cleaner in this amplifier stage filters the amplified spontaneous emission (ASE) and pre-pulses to enhance the temporal contrast to 10^{-8} (nanosecond time-scale). The 10-Hz pulse after the pulse cleaner is amplified in a pre-amplifier stage and then two power amplifier that boost the energy to 50 mJ, 2 J and 5 J respectively. The beam from the 5-J amplifier is expanded to 3 in diameter and compressed to - 30 fs by a four-pass, two-grating compressor. The compressed pulse energy is 3.5 J, which corresponds to > 100 TW peak power at 10 Hz repetition rate. For PW operation, the 5-J output with 3 in diameter is amplified in the final amplifier to >40 J. This amplifier is pumped by 4 Nd: Glass lasers (ATLAS PLUS, THALES LASER) each producing 25 J at 527 nm with a repetition rate of 0.1 Hz. The beam profiles of all the 25-J pump lasers are smoothed to perfect flattop with beam homogenizers. The gain medium for the PW stage is a 115-mrn diameter Ti:sapphire crystal, with a cladding of index-matching liquid, and absorption dye, used to avoid the transverse spontaneous emission or parasitic lasing due to the high-energy pumping [3]. The 10 Hz output is stepped down in repetition rate, synchronized with the pumps and amplified to >40 J. The amplified pulse is expanded to 7 in and compressed to PW level peak power is a separate four-pass, two-grating compressor. For the work reported here, we used several configurations comprised of 100 TW and 200 TW peak power with one or two pulse compressors being used.

1.1 Optimal focusing with adaptive feedback control

In a high power CPA system, wavefront distortion occurs because of the thermal effect in the high-energy amplification stages, especially with a repetition rate as high as 10 Hz. The large aperture optics for expanding the beam also introduce optical aberrations that contribute to the wavefront distortion. In both 100 TW and 1-PW beamlines, we employ aberration-free reflective parabolic telescopes to expand the beam before sending it to the compressor. Compared to a lens-based telescope, reflective expanders spherical aberration and eliminate chromatic aberration. The residual wavefront distortion can then be corrected by an adaptive optics system consisting of a deformable mirror and a wavefront sensor (SID4, PHASICS Inc.). Instead of using equivalent plane imaging, we used a direct measurement to correct for the wavefront distortion [1]. This was made possible by the ability of the wavefront sensor to measure a diverging beam. We could obtain an optimal focal spot by correcting for almost all the aberrations produced in the laser system. The deformable mirror (DM) (NIGHTN Ltd) was placed just after the compressor, and communicates with the wavefront sensor in a real-time close-loop feedback configuration. An off-axis parabolic mirror focuses the beam onto the target. A reflection off the front surface of a 45° uncoated wedge

is used to sample the beam. Therefore, the measured values were exactly the same as those on target. The wedge can be moved in for measurements, and out for high-power experiments. Microscope objectives (10X and 20X) and a 12-bit camera (Q-Imaging Inc.) were used in vacuum[1] to characterize the focal spot. The wavefront sensor was placed directly after the OAP. A band-pass filter (800±10 nm) was inserted before the wave-front sensor to eliminate chromatic aberration. The parabolic reflector was precisely aligned in air and any misalignment when the system is pumped down can be compensated by the DM. With this system in place the focal spot could be optimized to obtain near-diffraction limited spot size. A sequence of 10 consecutive focal spot measurement is shown in Fig. 1.

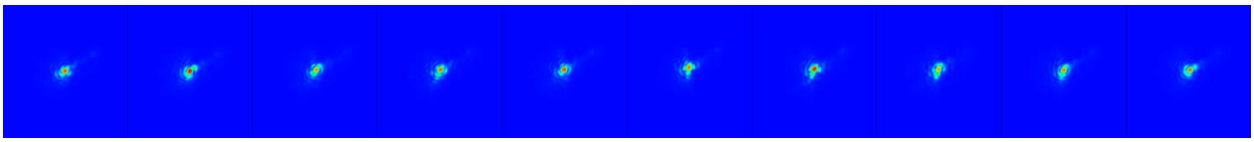

Figure 1: Sequence of 10 consecutive measurements of the focal spot of F/13.3 parabolic reflector. The incident wavefront is corrected with a closed loop system comprised of a wavefront sensor and deformable mirror.

The results of this measurement are analyzed using standard metrics. For the focal spot, the most important criterion for us is the enclosed energy in the central spot. For a flat-top beam profile, the theoretical limit is 70% if the $1/e^2$ Gaussian width is used. The results are shown on the left in Fig. 2. It indicates that the focusing is nearly optimal and the enclosed energy is close to the theoretical limit. Besides the quality of focusing, an important criterion is the pointing stability of the beam. The short-term pointing stability of the Diocles laser is excellent (~5 μrad). In the longer-term, the pointing stability is primarily determined by environmental effects. The laboratory has excellent temperature (±1 ^{o}F) and humidity control (±5 %) and the result is a laser system with minimal drift. The pointing stability has been measured to be 10's of μrad over 8 hours and this is shown on the right in Fig. 2.

Metric	Spot size (μm)	Enclosed energy (%)
Gaussian width ($1/e^2$)	X:35.2±8.3 Y:41.2±7.8	58±2
FWHM	X:20.8±2.3 Y:22.1±3.5	29.0±1.7

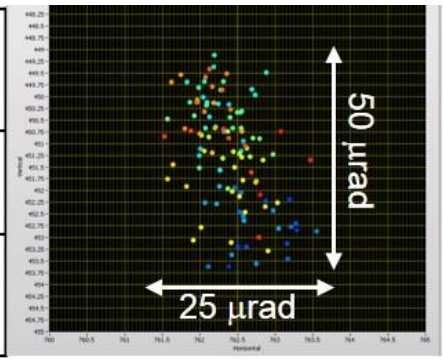

Figure 1: Left - computed parameters for the focal spot shown in Fig. 1. The enclosed energy in the Gaussian radius approaches 80% of the theoretical limit. Right – long term pointing stability of the Diocles laser system.

Adaptive control of the fundamental laser wavelength is fairly routine nowadays for high-power lasers. Of greater interest is wavefront control of the second harmonic. Radiation at 400 nm is interesting on account of the higher contrast as well as for generating high-energy photons from Thomson scattering. This radiation is fairly straightforward to generate using the process of second harmonic generation in a nonlinear crystal. The linear relationship between the phase aberration

[1] The "ON" time of the cameras was kept as short as possible (less than 10 minutes) to avoid the undesirable thermal effects (camera burnout).

of the second harmonic generated (SHG) light and the fundamental radiation ($\phi_{SHG} \approx 2\phi_{fund}$) makes it feasible to minimize wavefront aberrations of the SHG beam by correcting the wavefront of the fundamental beam. We recently demonstrated that such simultaneous wavefront correction at two wavelengths is indeed possible. As a result, the focusability of both the 800-nm and 400-nm beams showed dramatic improvement[2].

The schematic of the experimental setup for SHG generation and wavefront correction is depicted in Fig. 3. A half-wave plate (HWP) and thin-film polarizers (TFPs) attenuation system is used before the compressor to sample the high-power, stretched pulse. This approach enables measurements to be done at lower power without altering the properties of the high-power beam. The attenuated pulse at 800 nm is compressed to 34 fs using a grating pulse compressor. A bimorph deformable mirror (NightN) located after the compressor is used to correct the distortions in the laser pulse. The corrected pulse is then focused by an off-axis parabolic reflector with a focal length of 1 meter. The beam diameter on the paraboloid surface is 60 mm. The focused beam is reflected off mirror M1 and incident on a lithium triborate (LBO) crystal placed before the focus, as shown in Fig. 3. LBO was chosen as the frequency-doubling crystal because of its high nonlinear coefficient, high damage threshold, and the fact that it can be manufactured in large sizes (>100 mm). The uncoated LBO crystal was cut to 0.5 mm thick with type I phase matching, and the beam size on the surface of the LBO crystal was 9.5 mm. The beam was then reflected by an uncoated wedge to further attenuate the beam energy. We used a four-wave shearing interferometer device (SID4, Phasics Inc.) as the wavefront sensor to measure the wavefront. The SID4 was placed after the focus to measure the aberration from the entire system, including that from the parabolic mirror. The deformable mirror is within the depth of field of the SID4 imaging system. The focal spot was measured by inserting a silver mirror (M2) before the focus and imaging the focal plane using a 20X microscope objective and a 12-bit CCD camera. The energy in the second harmonic beam is measured by replacing the wedge with a dichroic mirror (HR@400 nm & HT@800 nm) and using a calibrated photodiode.

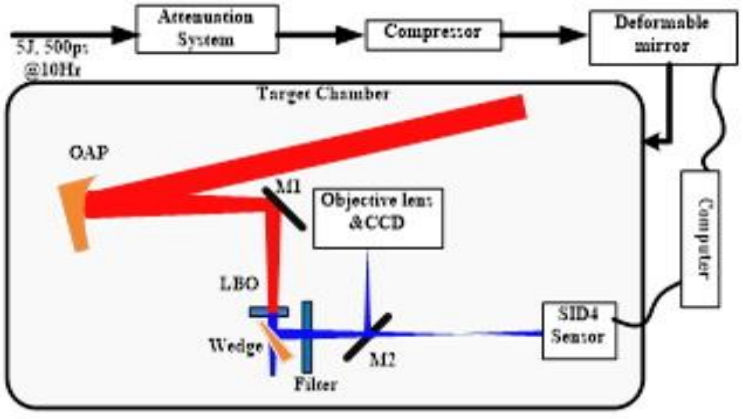

Figure 2: Schematic of the experimental setup for SHG generation, and measurement of the laser-light wavefront and focal spot size. The high power beam is sampled using a wedge, the wavefront is measured using the SID4 sensor and corrected with the deformable mirror. A 20X microscope objective is used to image the focus of the off-axis parabolic reflector to a 12-bit CCD.

[2] B. Zhao et al., "Wavefront-correction for nearly diffraction-limited focusing of dual-color laser beams to high intensities," Optics Express (submitted)

The focal spot quality is quantified by measurement of several parameters. The wavefront distortion for the uncorrected and corrected cases is specified by the peak-to-valley (PtV) and the root mean square deviation (RMS). The focal spot quality is quantified by the measurement of the spot size (FWHM), as well as the enclosed energy in the central spot. Based on the optimized focal spot size and the diffraction-limited focal spot size, the focusability of the beam was quantified by measurement of the enclosed energy in 10 μm (20 μm) diameter for 400-nm (800-nm) light.

In order to correct the wavefront, a feedback loop is implemented for the 400 nm light. This is accomplished by using a 400 nm interference filter in front of the CCD and performing the adaptive optic feedback correction of the incident wavefront. The results are shown in Fig. 4. The PtV and RMS value for the 400-nm wavefront distortion was 0.61 λ and 0.09 λ, respectively. The PtV and RMS value for the 800 nm-beam were 0.42 λ and 0.06 λ, respectively. Measurement of the focal spot indicates that 39.1% of the energy is contained in the central 20-μm diameter for the 800-nm beam, and 33.6% in the central 10-μm diameter for the 400-nm beam. The PtV, RMS, and enclosed energy values indicate that the aberrations in the 400-nm and 800-nm beams were both compensated simultaneously with use of the unconverted 800-nm loop or the 400-nm loop. Similar results are obtained when the unconverted 800 nm radiation is used for wavefront correction. These results will make it possible to perform two-color high-intensity experiments.

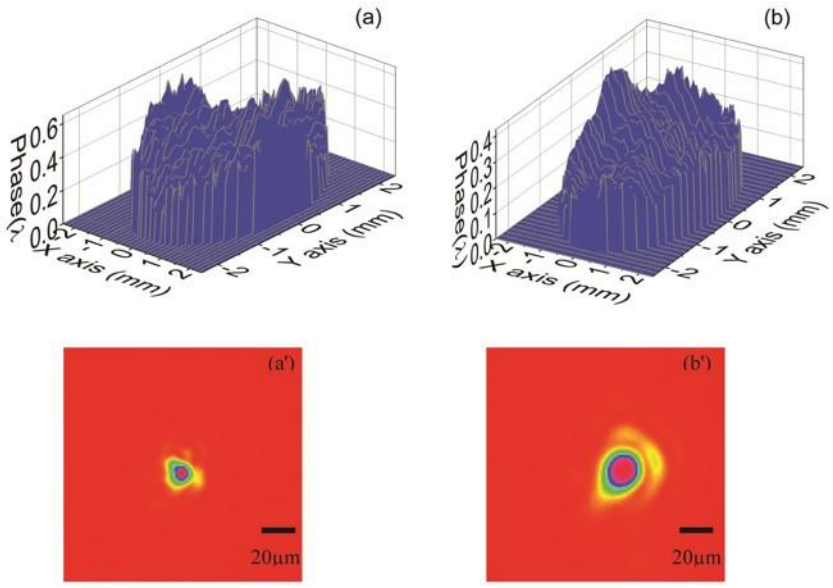

Figure 2: (a) Wavefront of 400-nm beam with 400-nm loop; (a') Focal spots of 400-nm beam with 400-nm loop; (b) Wavefront of 800-nm beam with 400-nm loop; (b') Focal spots of 800-nm beam with 400-nm loop.

1.2 Adaptive-feedback spectral-phase control for transform limited pulses

The spectral phase, which determines the temporal pulse shape, is a critical laser parameter that needs to be controlled and optimized for the high intensity laser matter interaction. As the spectral phase also controls the pulse temporal contrast ratio, it affects the results in high-field physics experiments due to the pre-ionization [4]. Interactions that depend on the carrier frequency, which are affected by laser pulse chirp, also require spectral phase control. In terms of the CPA laser pulse compression, it is difficult to remove all of the high-order phase distortions by only tuning the stretcher/compressor parameters. Several technologies have recently been demonstrated to precisely control the spectral phase for ultrafast laser pulses. In particular, an adaptive spectral

phase closed-loop feedback system has the capability to measure the spectral phase using a self-referenced spectral interferometer (SRSI), and it is able to precisely control the spectral phase by means of an acoustic optic programmable dispersive filter (AOPDF) [5]. Experiments that use high-power laser pulses must be performed in vacuum in order to prevent degradation of the laser pulse on account of nonlinear effects during propagation in air. However, the current spectral phase control methods which are used under atmospheric and low-power conditions are not compatible with high-field experiments. Therefore, a complete and systematic method is imperative to fully characterize and control the spectral phase and temporal shape of the on-target high-power pulses for high-field physics experiments under vacuum conditions.

We have demonstrated an adaptive closed-loop system that controls the spectral phase of laser pulses from a 100 TW laser system. Pulses with both ideal temporal shape and enhanced coherent contrast were obtained at the location of the target in vacuum. The high-power laser beam was then transported into the experimental vacuum chamber. A part of the beam from the off-axis parabolic reflector that focuses the beam on target was reflected by a wedge. This was guided to the measurement device by means of a convex mirror and a plane mirror assembly that down collimates the beam to the desired diameter. The beam exits a window in the vacuum chamber to the measurement device. The dispersion of the window was accounted for in measurements of the temporal pulse duration. For these measurements the B-integral was not a concern since all reflective optics were used. The pulse energy was attenuated to less than 100 μJ by the attenuation system without altering the temporal and spectral properties of the high-power laser pulse. The spectral phase was measured using SRSI (Wizzler, Fastlite Inc.) for each laser shot. The spectral phase information was extracted from the spectral interference between the initial pulse and its crossed-polarized wave (XPW) pulse. An adaptive spectral phase closed-loop between the SRSI and AOPDF, using the measurement from the SRSI to set the phase imparted by the AOPDF on the pulse, was implemented in order to compensate for the residual dispersion from the entire laser system. With the feedback loop in operation, the SRSI was used to measure the temporal pulse duration. The result of this measurement is shown in Fig. 5(a), and the pulse duration was 32 fs. This is in agreement with the Fourier-transform limited (FTL) pulse duration that is expected based on the spectral shape and bandwidth of the incident laser pulse [6].

An independent measurement of the pulse duration was performed using the technique of frequency-resolved optical gating (FROG) (GRENOUILLE, Swamp Optics), and the results are shown in the left inset of Fig. 5(a). This measurement results in a measured value of 32 fs for the pulse duration, which is in agreement with the SRSI measurement. Figure 5(b) shows the temporal profile of the pulse as measured by the Wizzler. In addition to obtaining an FTL pulse, the coherent contrast on the 400 fs timescale was improved by two orders of magnitude, when the spectral phase was corrected using the feedback system (CL), as compared to the optimal pulse duration without spectral phase correction (OL). The pulse duration in the latter case was 33 fs. This result represents a significant step forward compared to prior work that improved the coherent contrast on picosecond time scale by proper choice of stretcher optics. Such active feedback techniques will be critical in experiments where the coherent pedestal has undesirable effects on the target before its interaction with the high-intensity laser pulse. The spectral phase with adaptive spectral phase control as shown in Fig. 5(c) illustrates the spectrum of the laser pulse, the modulated spectral phase, and the flat phase that was obtained with feedback correction. The flat spectral phase corresponds to the FTL pulse in the temporal domain and this corresponds to compensation of all spectral orders that distort the phase during amplification and propagation in the laser chain. As noted above, both conditions produced nearly identical temporal durations, but the flat spectral

phase led to a significant suppression of the coherent pedestal on femtosecond time scales. Similar to the pulse duration which was independently measured using the FROG technique, we verified the validity of the measurement using independent techniques based on second harmonic generation (SHG) and XPW generation. The SHG and XPW spectra at the target point with different frequency chirp values were measured in vacuum. Figure 5(d) shows the SHG spectra for three different chirp values at -200 fs^2, 0, 200 fs^2. Zero chirp corresponds to the FTL pulse. The bandwidths of the SHG spectra were nearly identical for all three cases and maximum conversion efficiency was measured for FTL pulses. An XPW crystal (BaF_2, 1 mm long, (011)-cut) was also placed at the target point. Figure 5(c) shows the XPW spectra respectively at -200 fs^2, 0, and 200 fs^2. The spectra for the three frequency chirp values were all broadened by the XPW effect. We observed both the broadest spectrum and highest XPW conversion when there was no frequency chirp in the pulse. The measurements made with the SRSI, FROG, SHG, and XPW validate our claim that a transform-limited pulse was obtained at the interaction point.

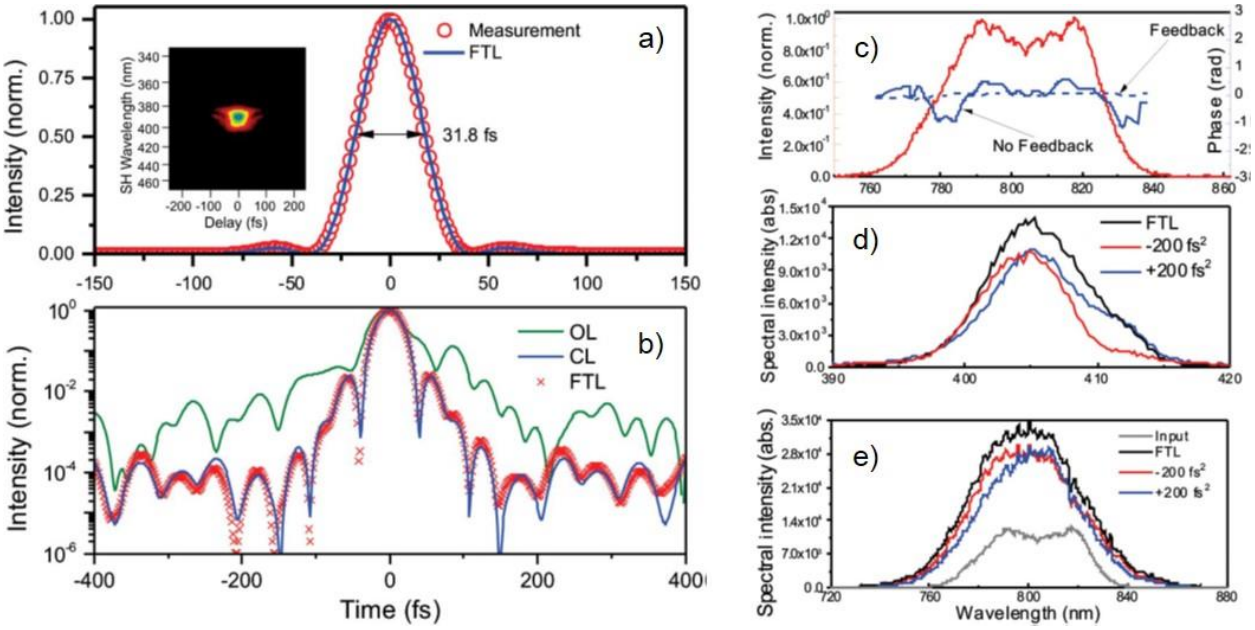

Figure 3: Measurement results of pulse duration and coherent contrast. (a) Temporal profile with spectral phase closed-loop. The upper-left inset shows the trace from the SHG FROG, which gives almost the same result of 32 fs. (b) Coherent contrast with feedback (CL), without feedback (OL), and the theoretical FTL pulse (FTL). Spectral properties of the on-target pulses. (a) Measurement spectrum (red line) and spectral phase before (solid blue line) and after (dashed blue line) feedback. (b) SHG and (c) XPW spectra for cross-checking the FTL pulse at the target point.

2. Laser-driven wakefield acceleration

2.1 Generation of Stable, tunable, quasimonoenergetic electron beams

In order to meet the stringent requirements of applications, such as laser plasma based x-ray sources, LPAs must produce GeV-scale energy [7], quasi-monoenergetic (QME) electron beams [8--10] without a large divergence, low energy, and polychromatic background. Suppressing the background is important to minimize the noise produced in interactions, and improve the quality of secondary x-ray radiation. Poorly collimated background electrons also represent a significant radiation hazard when an LPA operates at high repetition rates. The additional shielding required offsets one of the important advantages associated with LPAs. Reduction of the electron energy spread and elimination of the low-energy spectral tails naturally occur when electrons are self-

injected during a very short time interval, much shorter than the laser pulse transit time through the plasma. Theory and simulations suggest that controlling the evolution of the driving laser pulse can improve localization of electron injection, leading to the near elimination of the low-energy background [11]. Alternatively, matching the pulse for self-guiding (in a uniform plasma) and working close to the self-injection threshold can reduce backgrounds significantly [12,13]. Realization of this approach in the laboratory, however, appears to require very demanding laser pulse and target quality.

We demonstrate that the near-threshold regime can be accessed in a stable manner, yielding high electron-beam quality over a broad range of laser and plasma parameters [14]. Simulations indicate that (for the experiments discussed here) the threshold for self-injection is determined by the location of the nonlinear laser focus relative to the exit of the plasma rather than by the power threshold for relativistic self-focusing. The nearly Gaussian radial profile of the focused 25–60 TW laser beam and stable operation of the laser system allowed for maintaining the favorable focusing geometry over long series of shots, precisely locating the nonlinear focus in the 3 to 4 mm length plasma. Thus, location and duration of self-injection was well controlled, yielding tunable production of 130–430 MeV electron beams with narrow energy spread and minimal low-energy background. For some parameters, over long series of shots, electron beams were produced with the complete absence of low-energy background. The tunability of the beam energy and stability of the acceleration process demonstrated here are vital for radiation-physics applications.

The target was a high-density jet of neutral helium produced by a 3 or 4 mm-diameter supersonic Laval nozzle. The neutral density profile (characterized interferometrically) has half-millimeter-long symmetric down-ramps along the edges, and a 2 or 3 mm central flat region. The laser pulse was focused before the front edge of the nozzle [15]. The accelerated electrons exiting the plasma impinge on a fluorescent screen (LANEX) that was imaged with a 12-bit CCD. The absolute response of LANEX to electrons, calibrated using an 18 MeV radio-frequency linear accelerator (Siemens Primus), was used to obtain the charge in a specified energy interval. The sensitivity and dynamic range of the detection system depends on the dispersion and angular divergence. For the conditions reported in this work, the achievable dynamic range exceeds 10^3 for beam divergence in the range of 3–5 mrad. Electron energy was measured using a magnetic spectrometer operating in a slit-free geometry and having a range of 20–500 MeV. The energy resolution was better than 10% at 300 MeV, and rapidly degraded beyond 400 MeV. The spectrometer response function has been modeled with the General Particle Tracer (GPT) code. The final energy distribution was obtained taking into account the finite beam divergence.

The lowest laser power at which QME electron beams could be reliably obtained with the 3 mm jet was found to be 26 TW. At this power, no accelerated electrons were detected below $n_e=9\times10^{18}$ cm^{-3}. LANEX images of magnetically dispersed electron beams in Fig. 6 (left and middle columns) show the progress from a broad, thermal-like electron energy distribution towards the spectrum with the QME peak at approximately 120 MeV. This transition, occurring as the density drops can be partly understood as a transition from the ‘‘self-modulated’’ regime with injection and acceleration occurring in several subsequent buckets to the standard blowout regime with injection and acceleration in a single bucket immediately trailing the laser pulse. Reduction of the plasma density increases the dephasing length, reduces the rate of pulse depletion, and mitigates undesirable nonlinear optical phenomena (such as optical shock formation), thus increasing both electron-beam energy and quality. Fig. 6 (right column) shows LANEX images of magnetically dispersed beams and corresponding lineouts for representative shots taken with the 43 TW pulse

for a range of plasma densities. Over the entire range of densities, the electron energy spectra show either weak or no background, with the QME component being the dominant spectral feature. The peak of the QME distribution is 320 MeV for the lowest density of this sequence and decreases to 130 MeV for the highest density.

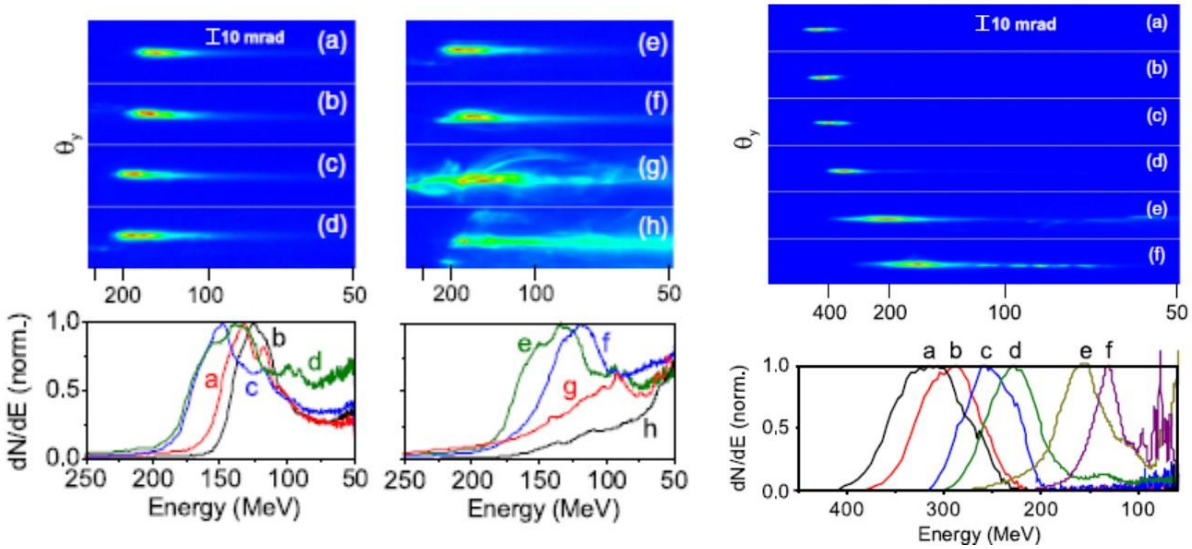

Figure 4: Left and center columns: Electron energy spectra obtained for laser power of 26 TW; the color scale is normalized for each shot. The left column [panels (a)–(d) and the plot at the bottom] shows LANEX images and corresponding lineouts for the lowest plasma density yielding stable, QME electron beams. The right column [panels (e)–(h)] shows that the electron spectra evolve from QME to quasithermal distributions as the plasma density increases. Right Column: QME electron spectra as a function of plasma density for the laser power of 43 TW.

One important benefit of the near-threshold regime is that the background-free beams are often observed in long series of shots; one representative series is shown in Fig. 7. Electron spectra shown in Fig. 7 have, on average, 29% normalized FWHM. The spectral peak corresponds, on average, to the 321 MeV energy, with a 22 MeV standard deviation over the series of shots. This deviation is better than the experimental uncertainty brought about by the coarse spectrometer resolution (~10% for E~300 MeV). The mean integrated charge is 7.16 pC with a standard deviation of 2.03 pC. Remarkably, within a resolution of the energy measurement, there is no evidence of correlation of electron energy with charge. This is consistent with the simulation data for similar regimes, showing that, to cause observable manifestation of beam loading (viz. more than 10% reduction of electron energy), and the injected charge should be at least an order of magnitude higher. The dynamics of self-injection process are explored by means of the 3D PIC code CALDER-CIRC and the numerically computed electron spectrum is in excellent agreement with the experimentally measurements.

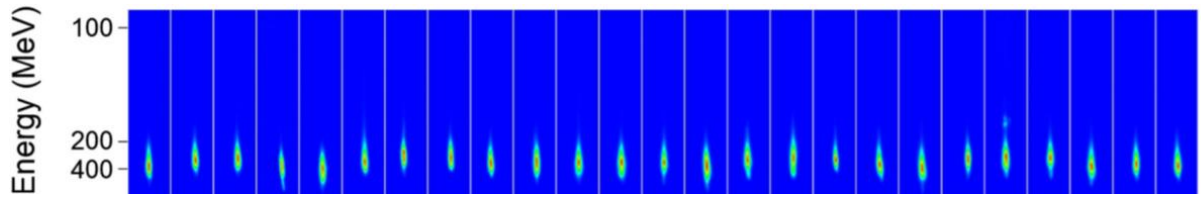

Figure 5: Image of the electron beam after dispersion in a magnetic spectrometer on a fluorescent screen (LANEX) for 25 consecutive shots. The laser power used is 55 TW. The beams have an average divergence of 3 mrad and a pointing fluctuation of ±1 mrad.

2.2 High-charge beams with mixed gas targets

In order to produce electron beams with higher charge, mixed gas targets (99% He + 1% N_2) are used for the generation of high-energy electron beams [16,17]. In the simplest implementation, a 2-mm supersonic nozzle is used to produce a high density gas flow (n_e=10^{19} cm^{-3}) and the drive pulse is focused onto the front edge of the flow. At the intensities used, the medium is fully ionized by the foot of the laser pulse [18]. The peak of the pulse is self-guided in the medium, drives a wake in the underdense plasma, and electron beams are produced by the ionization injection mechanism. Under optimal conditions, beams with cutoff energy <300 MeV are produced with charge ~100 pC for energy > 50 MeV. A sequence of 20 shots for this accelerator is shown in Fig. 8 and illustrates that the accelerator operates in a stable regime with reproducible shot-to-shot characteristics.

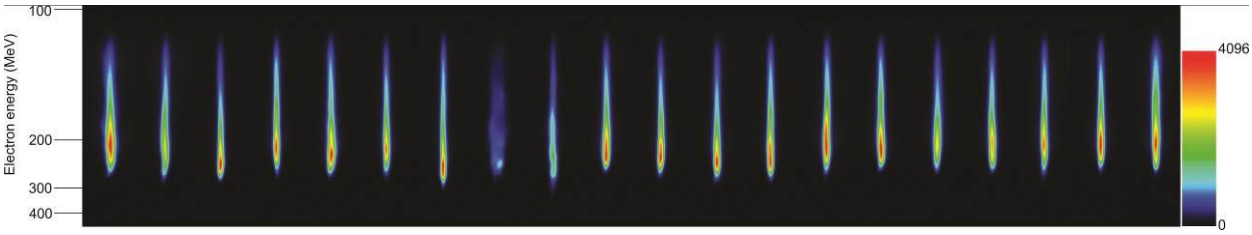

Figure 6: Spectra of electron beam from the laser wakefield accelerator. The data shown is for 20 consecutive shots. The energy spectra are polychromatic with a cutoff energy ~250 MeV and total charge of 0.1 nC (>50 MeV)

2.3 Tunable, quasi-monoenergetic beams with structures targets

Self-trapping produces e-beams with narrow energy spreads, but only over a restricted set of laser-plasma parameter combinations (laser intensity, laser focal position, plasma density, and plasma length). These stringent conditions are difficult to meet and maintain because of the nonlinear behavior and interdependence of the mechanisms involved. We overcame these limitations by using a novel target composed of two jets. This target provided us the ability to tailor the density and shape of the flow, and thereby decouple the injection and acceleration processes. We could then control each of them independently[3]. A single laser pulse was focused onto a single continuous gas target with independently adjustable gradient profiles of gas density and atomic composition, as shown in Fig. 9(a). By systematically varying these profiles, we were able to find the optimal ones for generating stable, quasi-monoenergetic, and tunable e-beams, while also holding constant both the electron charge and energy spread[4]. The resulting electron beam characteristics are shown in Fig. 9(b).

[3] G. Golovin et al. (to be submitted)
[4] G. Golovin et al., Physical Review Letters (submitted)

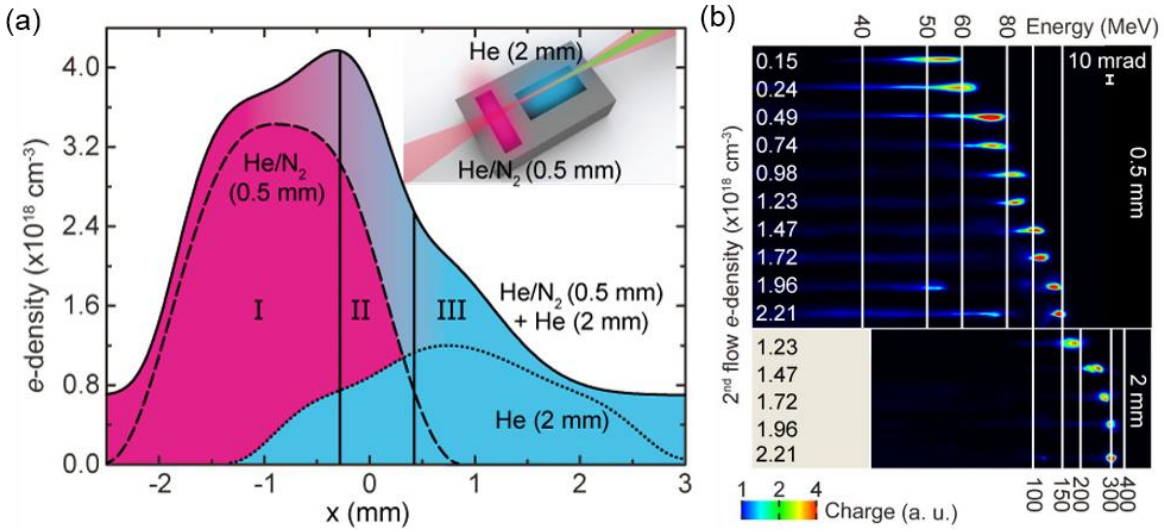

Figure 7: (a) Gas target profiles, measured using tomography, at a height of 2 mm above the nozzle orifices. The target is composed of helium with a small concentration of N2. Roman numerals indicate different regions of the optimal composite profile with the bubble being formed in region (I), electrons injected in (II), and accelerated to high energy in (III). The inset shows the orientation of the laser pulse propagation with respect to the gas target. (b) Images of the dispersed e-beams for different plasma densities show that the beam can be tuned over a large energy range. Two different accelerating structures are used to produce low and high-energy beams, with operating conditions chosen such that the beam charge and energy spread are nearly invariant.

To gain insight into the injection and acceleration processes, we performed simulations in 2-D slab geometry using OSIRIS PIC-code [19]. We used 100-μm x 200-μm simulation box, with 0.015625-μm x 0.25-μm cell size, and 8 simulation particles in each cell initially. The time interval between the two steps was 0.052 fs. We utilized the moving window technique, so that a relatively small simulation box could represent a large acceleration distance. The laser beam was 0.8-μm wavelength, 33-fs pulse duration, Gaussian beam mode, with a waist of 18.69 μm, a normalized vector potential of $a_0 = 2.5$, and focused at the overlap of the two gas flows. The gas-target profile was set to be the fitting result of the tomography measurement (see Fig. 9(a), *e*-densities for the first and the second flows are 3.4×10^{18} and 1.2×10^{18} cm^{-3}, respectively), which was approximated by the summation of super-Gaussian and Gaussian functions. The simulation stopped at the exit of the second flow, where the gas density was low enough that neither further acceleration nor phase-space evolution were observed.

The simulations show that all accelerated electrons originated from the ionization of nitrogen. The electrons born from helium contributed to a low energy background, and were not accelerated. This correlates with our experimental observations, and confirms the major role of the ionization-assisted injection. The simulations show a quasi-monoenergetic spectrum of the simulated *e*-beam, with a central energy of ~200 MeV, and FWHM energy spread of ~50 MeV. This is in good agreement with experimentally measured central energy (170±30 MeV), and energy spread (50±15 MeV). Further, the electrons constituting quasi-monoenergetic peak at 200 MeV were primarily injected in the 0-0.4-mm region, which corresponds to Region II of the gas target profile. It confirms the localization of injection in this region. By comparing energy spread immediately after injection terminated (at ~0.4 mm) to that at the end of the acceleration, we found that phase-space rotation decreased the absolute energy spread by a factor of two.

2.4 Control of electron beam using spectral chirp

Since we were able to obtain a flat phase laser pulse on the target and control the different order phases separately using the adaptive phase control method (see Sec. 2.3), this enabled us to study the dependence of laser-wakefield accelerated electron beams on the laser chirp without ambiguity [20]. A 2.4 J laser pulse was focused on a 0.5 mm mixed gas target (1% nitrogen and 99% helium) with an intensity of 5×10^{19} W cm^{-2}. Electrons were injected into a laser wakefield via an ionization assisted injection mechanism. The chirp of the laser pulse was changed from −600 fs^2 to 1000 fs^2. The typical electron beam energy spectrum generated at each chirp is shown in Fig. 10. This result revealed that a positive chirp helps to generate an electron beam with higher cutoff energy and charge. For this experiment, 200 fs^2 was the best chirp parameter for electron beam generation. The asymmetrical behavior of the electron energy and charge showed that the frequency chirp played a critical role in LWFA. While the detailed physics of this type of dependence will be discussed in a forthcoming report, this phase dependence experiment demonstrates the importance of this phase control technology in the study of high-intensity laser-plasma interaction [6].

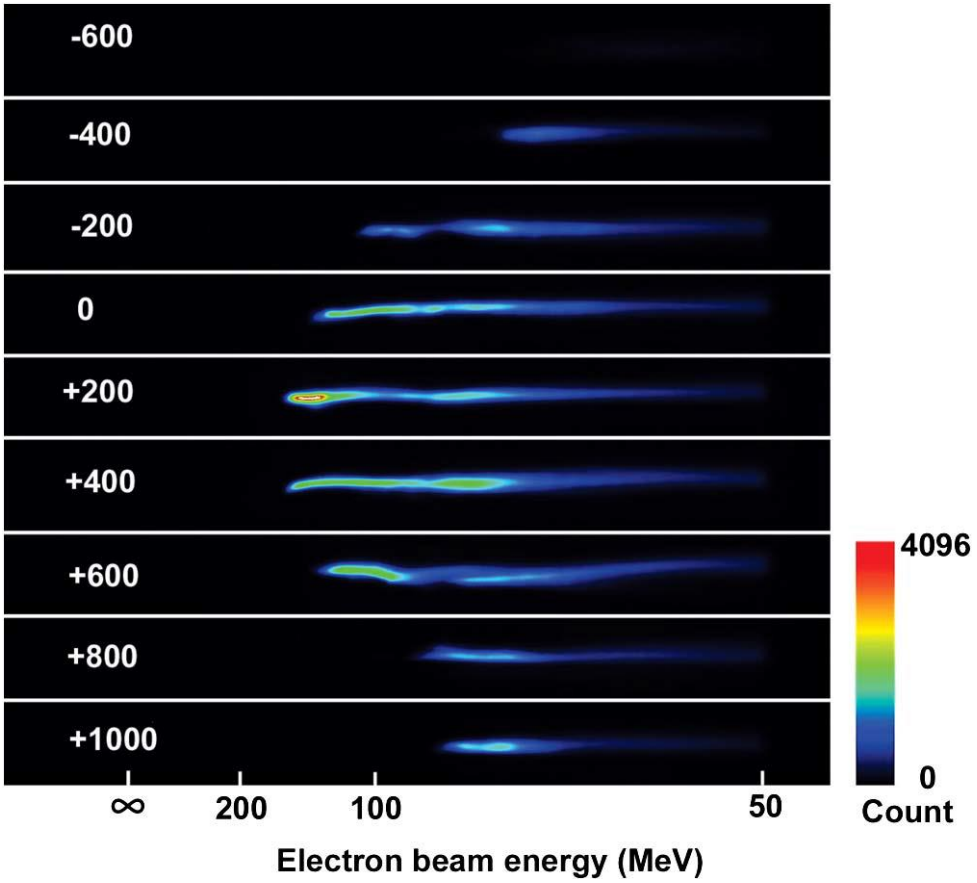

Figure 8: Dependence of laser chirp on the generation of quasimonoenergetic electron beams. The pulse chirp was scanned from −600 fs^2 to 1000 fs^2 while fixing other laser and accelerator parameters. It shows that the electron beam cutoff energy and charge above 50 MeV is asymmetric with respect to the zero chirp.

3. Laser-driven x-ray source

Recent breakthroughs in the generation of high-quality electron beams from laser-driven wakefield accelerators have made it possible to develop a table-top device capable of generating narrowband, collimated MeV x-ray beams. This novel x-ray source at UNL uses the process of inverse Compton

scattering—in which a high-energy electron beam scatters off an intense laser pulse—to produce a forward directed beam of energetic x-rays [21,22]. Two high-intensity laser pulses comprise the all-optical architecture. One laser pulse is focused to relativistic intensity and interacts with a supersonic gas jet to generate quasi-monoenergetic electron beams by the process of laser wakefield acceleration [23]. The second laser pulse, focused to high-intensity, scatters off the electron beam. The double Doppler shift associated with this process leads to a boost in the energy of the incident near-infrared light photons to x-ray wavelengths [24].

3.1 Broadband Thomson radiation

In the first implementation, we scattered a high-intensity laser pulse off a polychromatic electron beam from a mixed gas target (Fig. 8). The scattering laser pulse with 0.5 J is focused by a 1-m focusing lens. On account of dispersion in the beamsplitter, the pulse duration is 120 fs and b-integral effects lead to a focal spot with 22 μm diameter (FWHM) and 16% enclosed energy in the central spot. The corresponding intensity at the focus of the scattering pulse is 3×10^{17} W cm^{-2}, the associated normalized vector potential a_0 is 0.4, and the interaction is therefore in the linear regime. Spatio-temporal overlap of the beams is accomplished in several steps. First, the wakefield accelerator is optimized to ensure that the laser and electron beam are co-propagating. Optical techniques are then utilized to spatially overlap the two foci at the exit of the jet. For these experiments, the interaction point is chosen to be 1-mm downstream of the nozzle to ensure that focusing of the scattering pulse is not affected by the target. At this location, the transverse size of the electron beam and the focused scattering pulse are nearly matched. The pointing fluctuation of the high-power laser pulse on target is 5 μrad, and the angular jitter of the electron beam is 5-10 mrad. Temporal overlap is obtained by means of spectral interference between the drive and scattering pulses. The layout of the x-ray source is shown in Fig. 11.

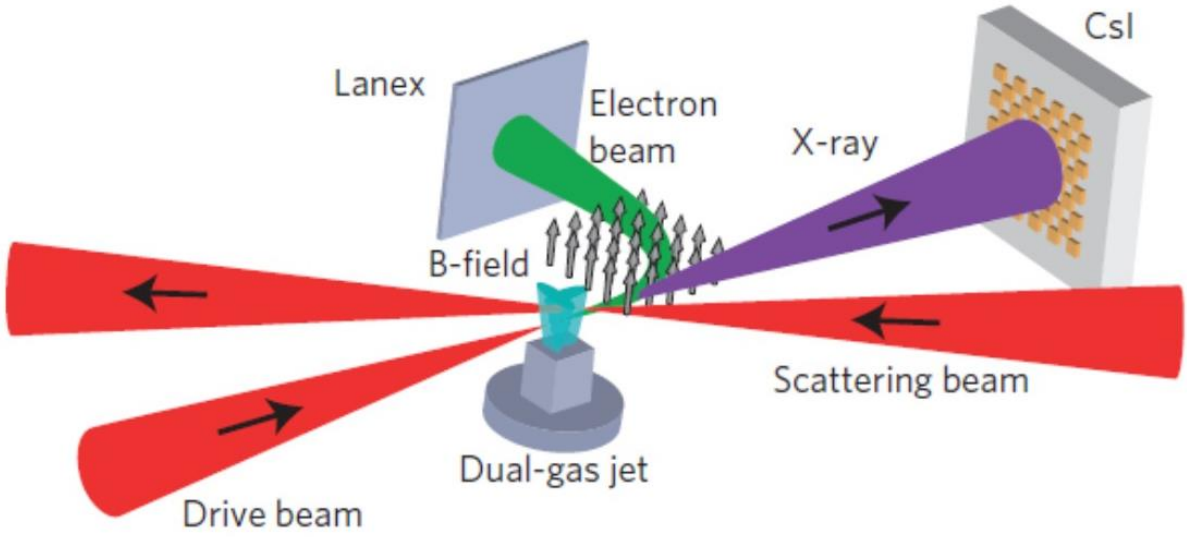

Figure 9: Experimental set-up (not to scale). Electrons (green) are accelerated by the interaction of a drive laser beam (red, from left to right) with a plasma created within the plume of a dual-stage gas jet and then deflected to a LANEX screen. A second laser pulse (red, from right to left) scatters from the electron beam after the accelerator. The X-ray beam (purple) is recorded by a CsI detector.

Under these experimental conditions, the interaction of the high-power laser pulse with the laser-driven electron beam results in generation of a forward directed beam of high-energy x-rays. These are imaged by the voxelated detector; a typical profile of the beam is shown in Fig. 12(a). Based

on this measurement and the detection geometry, it is inferred that the angular divergence of the beam is 12 mrad. A simple attenuation measurement is then performed to determine the spectrum of the high-energy x-ray beam. Three different thicknesses of lead are used in a quadrant geometry to cover different sections of the beam as shown in Fig. 12(b). A detailed numerical model that takes into account the spatial profile of the focused scattering pulse is used to compute the spectrum of the scattered x-rays. The distribution of electrons in phase space is constructed using the measured angular profile and the energy spectrum of the electron beam. Based on these calculations, the angle-dependent spectrum of the x-rays is determined. The spectral distribution as a function of laboratory observation angle is shown in Fig. 12(c). Using the computed spectrum at different angles, the transmission through each quadrant can then be computed and they are in excellent agreement with the measured transmission. Based on the absolute response, it is determined that 108 photons s-1 are produced at 10 Hz repetition rate. The size of the x-ray source is measured using a cross-correlation technique in which the scattering pulse is scanned along the vertical direction and samples different parts of the electron beam. The size of the x-ray source using this technique is found to be 5 μm. Based on prior studies measuring the temporal duration of the electron beam under the same conditions as this experiment, the peak spectral brightness is 2×10^{19} photons s^{-1} mm^{-2} $mrad^{-2}$ (0.1% BW) [25]. This brightness is nearly four orders of magnitude higher than from inverse Compton sources based on the scattering of a high-intensity laser pulse off an electron beam produced by a conventional accelerator[22].

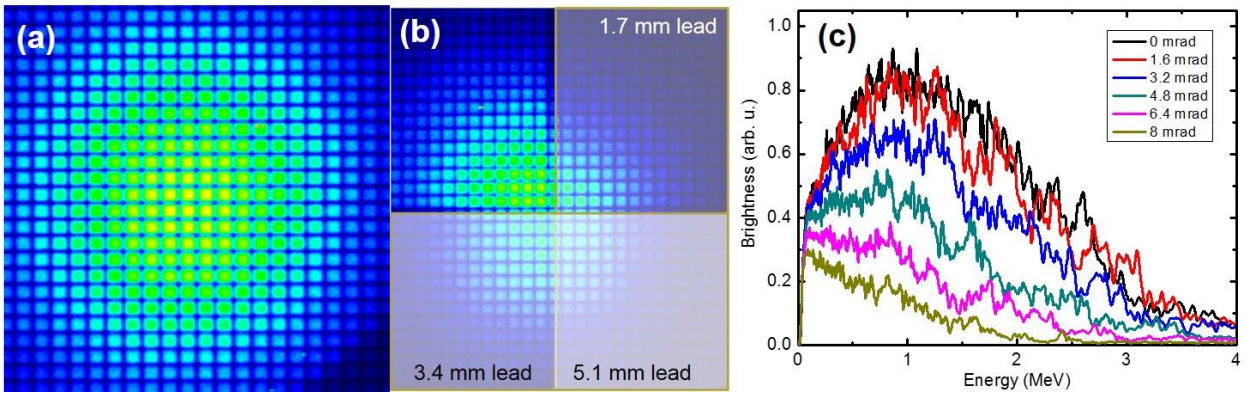

Figure 10: Spatial and spectral characteristics of the x-ray beam measured using the CsI array. The angular profile of the beam is shown in (a) with angular divergence of 12 mrad. (b) The energy of the x-ray beam is inferred by the use of attenuating filters and measurement of the net transmission through each quadrant. (c) The expected spectrum of the x-rays is computed using a numerical model and the measured and computed transmissions are in excellent agreement.

3.2 Narrowband MeV x-ray source

In order to generate narrowband and tunable x-rays, the electron beam spectrum needs to have small energy spread and be tunable over a broad range. This was achieved using the novel dual gas target described previously, and it enabled the generation of quasi-monoenergetic electron beams spanning 50-300 MeV. The scattering of these electrons with a high-intensity laser pulse produces quasi-monoenergetic x-ray beams, representing a significant advance over prior work using betatron emission [26]as well as Compton scattering that produced broadband x-ray spectrum [27].

Several methods can be used to precisely measure the energy spread of the x-ray beam, such as Compton scattering, single photon spectroscopy, or x-ray transmission. We implemented the Ross-

filter technique that relies on measurement of transmission through materials near the k-edge, as shown in Fig. 5 [28]. Since the highest k-edge available is 116 keV for uranium, the electron energy was tuned such that the peak photon energy would be <100 keV. A set of k-edges were chosen to correspond to the relevant energy for this measurement. The detection system was the voxelated CsI detector described previously. The filters were attached to the detector in a checkerboard pattern to yield multiple data points per shot as shown in Fig. 13(a). The thicknesses were carefully adjusted so that each filter pair would provide the precise photon number between the corresponding k-edges and no signal outside this band. The x-ray beam transmitted through the filters is shown in Fig. 13(b), and the profile of the filters can be seen imprinted on the beam. The results of this measurement are shown in Fig. 13(c-e). They show the results from three different conditions for the electron beam spectrum ranging from narrowband to polychromatic (red curves). The measured spectrum is shown by the black squares. The blue curves show the fit to the data using the model with the electron spectrum as input. The measurement and the predicted spectrum are in excellent agreement [29].

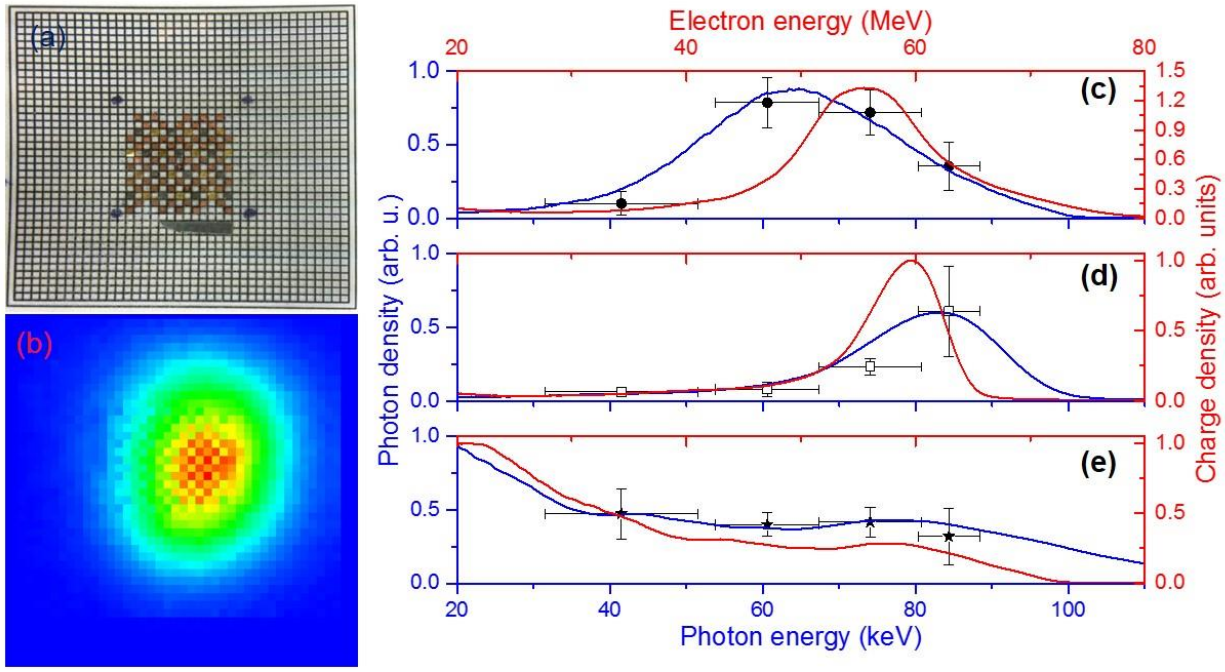

Figure 11: Measurement of the spectrum of narrowband x-rays using the Ross filter technique (a) checkerboard pattern of Ross filters on the CsI array (b) spatial profile of x-ray beam after transmission through the Ross filters (c)-(e) spectrum of x-rays measured using the Ross filters (black squares), measured electron beam spectrum (red curves) and computed x-ray spectrum (blue curves). The measured data points are in excellent agreement with the numerical model. Data shown in panel (c) is in absolute units: 10^7 photons MeV^{-1} Sr^{-1} for the x-ray beam and pC MeV^{-1} for electron beam.

The central x-ray energy was tuned over one order of magnitude by tuning the energy of the LWFA electron beams from 50 MeV to 300 MeV. A different filter set and analysis method were required to measure the x-ray photon energy over this much larger range due to the limited working range of the Ross-filter technique. The central x-ray central energy was observed to follow a quadratic scaling with the average electron-beam central energy, as the latter was tuned. This agrees with the theoretically predicted $E_\gamma=4\gamma^2E_L$ scaling for photons backscattered on-axis by a single electron, where E_L and E_γ are the scattering laser and scattered x-ray photon energies, respectively, and γ is the relativistic Lorentz factor of the electron.

The reproducibility and stability of the x-rays were also computed: x-ray beams are produced >90% of the time and monoenergetic beams ~50% as shown in Fig. 14. The x-ray photon number was stable to within 60% of its average value, 1.7 $\times 10^6$. The photon number, and thus photon flux, depends on three factors: scattering-laser beam intensity, degree of beam overlap and electron-beam charge. The stability was dominated by the stability of the electron-beam charge, which for this data set was stable to within 45% of its average value, 29 pC. Greater control of the flux can be achieved by stabilizing the electron-beam charge and adjusting the scattering-beam intensity.

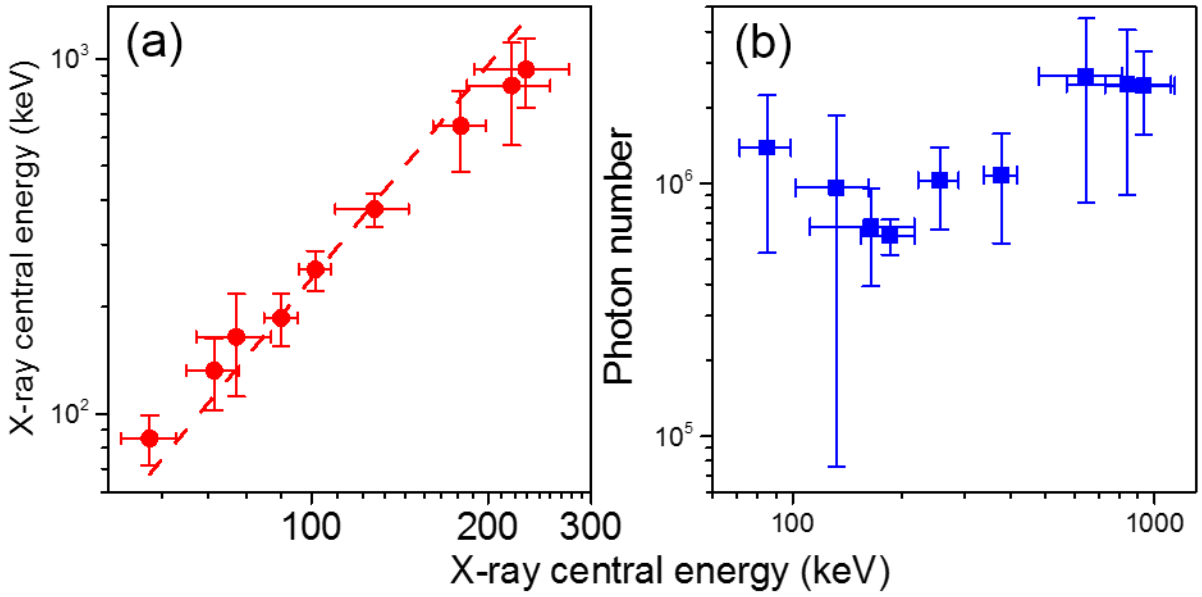

Figure 12: Measured x-ray central energy (red circles), plotted versus the measured electron-beam central energy, and is consistent with a $4\gamma^2$ scaling (red dashed line). Error bars represent 80% confidence intervals, calculated using the t-distribution of measurements of the set. (b) The average photon number/shot, measured for plotted as a function of the average central energy of the x-ray beam. Across an order-of-magnitude range of x-ray energy, the x-ray photon number is found to be stable to within 60% of its average value, 1.7×10^6.

The size of the x-ray source is measured using a cross-correlation technique in which the scattering pulse is scanned along the vertical direction and samples different parts of the electron beam. The size of the x-ray source using this technique is found to be 5 μm. Based on prior studies measuring the temporal duration of the electron beam under the same experimental conditions, the peak spectral brightness is 2×10^{19} photons s^{-1} mm^{-2} $mrad^{-2}$ (0.1% BW). This brightness is nearly four orders of magnitude higher than from inverse Compton sources based on the scattering of a high-intensity laser pulse off an electron beam produced by a conventional accelerator.

3.3 Generation of x-ray beams above the photonuclear threshold

We have also demonstrated that this source can operate in an energy range that is relevant to photonuclear physics. The photofission threshold of actinides is ~6 MeV while the threshold for (γ, n) reactions is ~8 MeV. The increase in scattered photon energy was accomplished by upconverting the incident laser light using second harmonic generation in a KDP crystal. As a result, the scattered x-ray frequency is upshifted by a factor of two. The same effect can be accomplished by using a higher electron energy. The architecture of the source was upgraded by the use of two pulse compressors to independently compress and optimize the temporal characteristics of the scattering pulse. Aberration in the crystal and the incident beam as well as

nonlinear effects during the harmonic conversion process led to degradation of the 400 nm focus. A trade-off was found between the pulse duration and focusability, and it was empirically determined that for a pulse duration of 300 fs, the focusability of the 400 nm was acceptable. Further improvements to this device are planned by the inclusion of a separate adaptive optic to the scattering beamline in order to obtain optimal focus for the 400 nm pulse. A more sophisticated detection and analysis system was used by imaging the scattered x-rays using two CsI arrays. The x-ray beam was incident on the 1-cm thick CsI array, and the transmitted x-rays were then propagated through a custom filter and incident on a second CsI array with 2-cm thickness. The first array measured the spatial profile and pointing of the beam while the second array was used for measurement of the x-ray photon energy. The transmission of the x-ray beam through a specially designed filter was used to infer the energy of the x-rays. This measurement was validated by computing the scattered photon spectrum and comparing the predicted transmission to the measurement. The results of this measurement are shown in Fig. 15 and demonstrate the generation of photon beams with mean energy of 9 MeV and extending to 15 MeV. Based on the γ-ray spectrum and the known CsI detector response, it is inferred that 3×10^5 γ-ray photons per shot were produced. The measured x-ray photon number is found to be approximately consistent with calculations using the measured parameters of the scattering laser beam and the electron beam, and assuming non-ideal spatial overlap of the two beams (equal to ~1⁄3 of their beam diameters), which may arise from their pointing fluctuations [30].

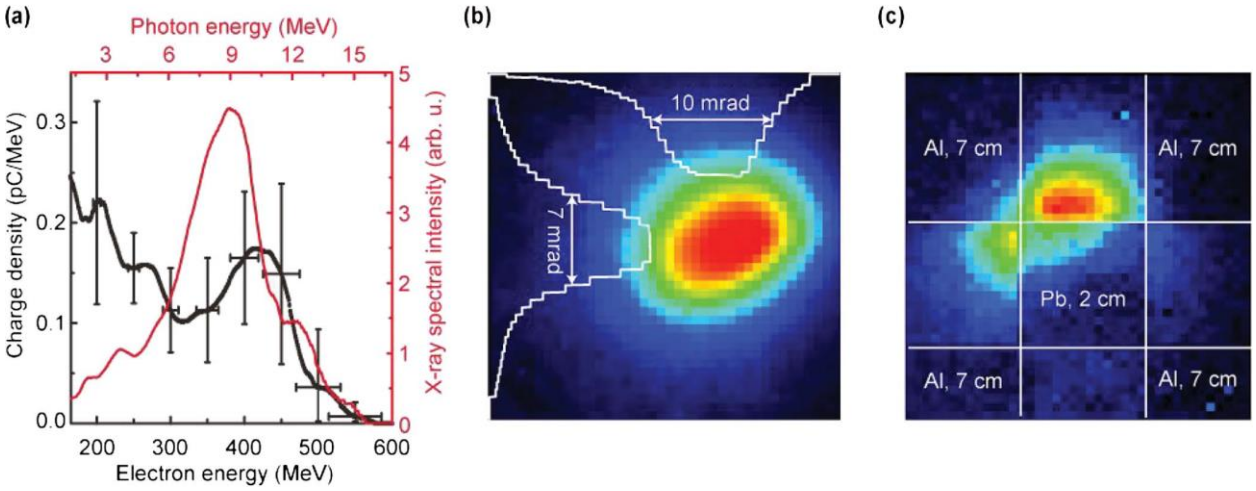

Figure 13: Electron and γ-ray characteristics. (a) Black curve—averaged electron beam spectrum. Red curve—corresponding estimated on-axis γ-ray spectral intensity (scattering laser pulse wavelength is 400 nm). (b) Measured signal on the CsI (background-corrected) with no spatial filter; γ-ray beam divergences (FWHM) are shown on the overlaid horizontal and vertical profiles. (c) Measured signal on the CsI (background-corrected). The overlay shows a spatial filter in front of the CsI, consisting of four blocks of aluminum (7 cm thick) and one block of lead (2 cm thick).

4. Theoretical and Numerical Results

4.1 Modeling of experimental results on the production of quasi-monoenergetic, background-free electron beams in the energy range 300-800 MeV.

Stable operation of the laser plasma accelerator near threshold for self-injection in the blowout regime has been demonstrated for the first time, using 40 - 60 TW, 30 fs, nearly Gaussian at focus (the spot radius 13.5 microns) drive pulse. Stable, well collimated, 250 - 430 MeV quasi-monoenergetic electron beams, with almost total absence of low-energy background, were observed over long series of shots in experiments with high-density gas-jet targets of 3 - 4 mm length and $n_0 = (5 - 7.2)\times10^{18}$ cm^{-3}. Background-free quasi-monoenergetic beams with the energies beyond 600 MeV were consistently produced from cm-length, low-density plasmas ($n_0 < 4\times10^{18}$ cm^{-3}) using 80 - 90 TW drive pulses.

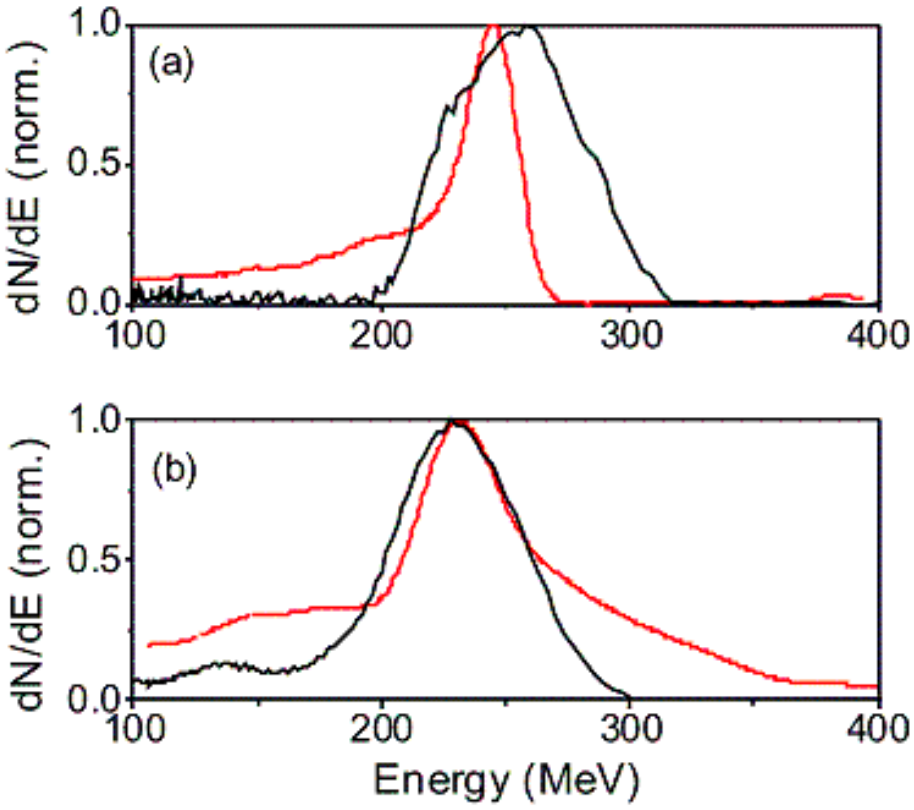

Figure 14: Lineouts of experimental (black), and simulated (red) electron energy spectra near threshold for self-injection: (a) P = 43 TW, $n_0 = 7.2\times10^{18}$ cm^{-3} and (b) P = 43 TW, $n_0 = 7.8\times10^{18}$ cm^{-3}. In the simulation, the laser pulse (Gaussian) was focused at a 1 mm distance before the edge of the plasma [2].

Combined reduced and full 3D particle in-cell simulations (using cylindrical quasi-static code WAKE and quasi-cylindrical code CALDER-Circ) explained the dynamic nature of the self-injection threshold. Observation of perfect electron beams from dense plasmas ($n_0 \approx 7\times10^{18}$ cm^{-3}) indicated that certain genuine features of acceleration process in high-density plasmas (viz. rapid formation of the bubble, causing rapid self-steepening of the drive pulse and subsequent continuous injection) were missing in the experiment. Production of the optimal beams in the laboratory was thus associated with the precise location of the laser pulse focus and transient dynamics of the pulse in a finite-length plasma, rather than with the stable self-guiding of the pulse

through electron dephasing and/or pulse depletion. It was shown that varying the position of the vacuum focal plane of the pulse with respect to the plasma target (gas jet) helped adjust the position of the nonlinear focus so as to control the location of electron blowout and electron injection within the finite-length plasma. Focusing the drive pulse before the plasma, within a range of experimental uncertainty, was shown to delay formation of the bubble until the rear half of the plasma. The electron beam with a small phase space volume was thus produced and accelerated through the remainder of the plasma, being released from the plasma before the continuous injection (caused by the drive pulse self-steepening) started to deteriorate the beam quality. Numerical modeling using the quasistatic WAKE code with fully dynamic test particles allowed for serial optimization runs, providing the guidance for the fully 3D PIC runs that retrieved the electron beams agreeing in energy and energy spread with those produced in the laboratory experiment (cf. also Figure 16), also retrieving the density threshold for self-injection. It was also shown that this plasma lens effect can be enhanced using layered gas targets (for instance, multiple gas jets) to control the nonlinear focusing without changing the position of the vacuum focal plane [CP3].

4.2 Computationally efficient methods for modeling laser wakefield acceleration in the blowout regime

Thorough benchmarking of the main simulation tools (Cartesian, fully explicit, 3D PIC code VORPAL with the perfect dispersion algorithm and quasi-cylindrical, fully explicit, 3D PIC code CALDER-Circ) had shown good agreement in terms of charge, energy, and energy spread of quasi-monoenergetic features, collection volumes, precisely reproducing the physical phenomena responsible for initiation and termination of self-injection. Either code can be thus used with high confidence to model electron acceleration through dephasing. Knowing collection volumes in advance from the fast hybrid simulations (using the WAKE code) allows to enhance macroparticle statistics in this volume, enabling future simulations with lower sampling noise and better retrieval of the fine structure of electron beam, simultaneously reducing the simulation cost (by more than 50%). The physical origin of continuous injection contaminating electron spectra with high-charge polychromatic background is identified: it is the driver pulse transformation into an optical shock with a sub wavelength-scale rising front. Preventing the shock formation (thus keeping the dark current low) appears to be possible using large-bandwidth negatively chirped pulse as a driver.

4.3 All-optical control of electron injection and acceleration in the LPA

Generation of background-free, polychromatic (comb-like) electron beams using laser plasma acceleration in longitudinally uniform, mm-length dense plasma channels.

The accelerating bucket of a laser-plasma accelerator (a cavity of electron density maintained by the laser pulse radiation pressure) evolves slowly, in lock-step with the optical driver, and readily traps background electrons. The trapping process can thus be controlled by purely optical means. Sharp gradients in the nonlinear refractive index produce a large frequency red-shift, localized at the leading edge of the pulse. Negative group velocity dispersion associated with the plasma response compresses the laser pulse into a relativistic optical shock (ROS), slowing the pulse (and the bucket), reducing the electron dephasing length, and limiting energy gain. Even more importantly, the ponderomotive force of the ROS causes the bucket to constantly expand, trapping copious unwanted electrons, polluting the electron spectrum with a high-charge, low-energy tail. We show that using a drive pulse with a bandwidth close to a one-half of the carrier wavelength provides effective dispersion compensation. The negatively chirped, ultrahigh bandwidth (up to

400 nm) drive pulse: prevents ROS formation through dephasing; extends the dephasing length; and almost completely suppresses continuous injection. High quality, GeV-scale electron beams can be thus produced with sub-100 TW lasers (rather than PW-class) in mm-scale (rather than cm-scale), high-density plasmas.

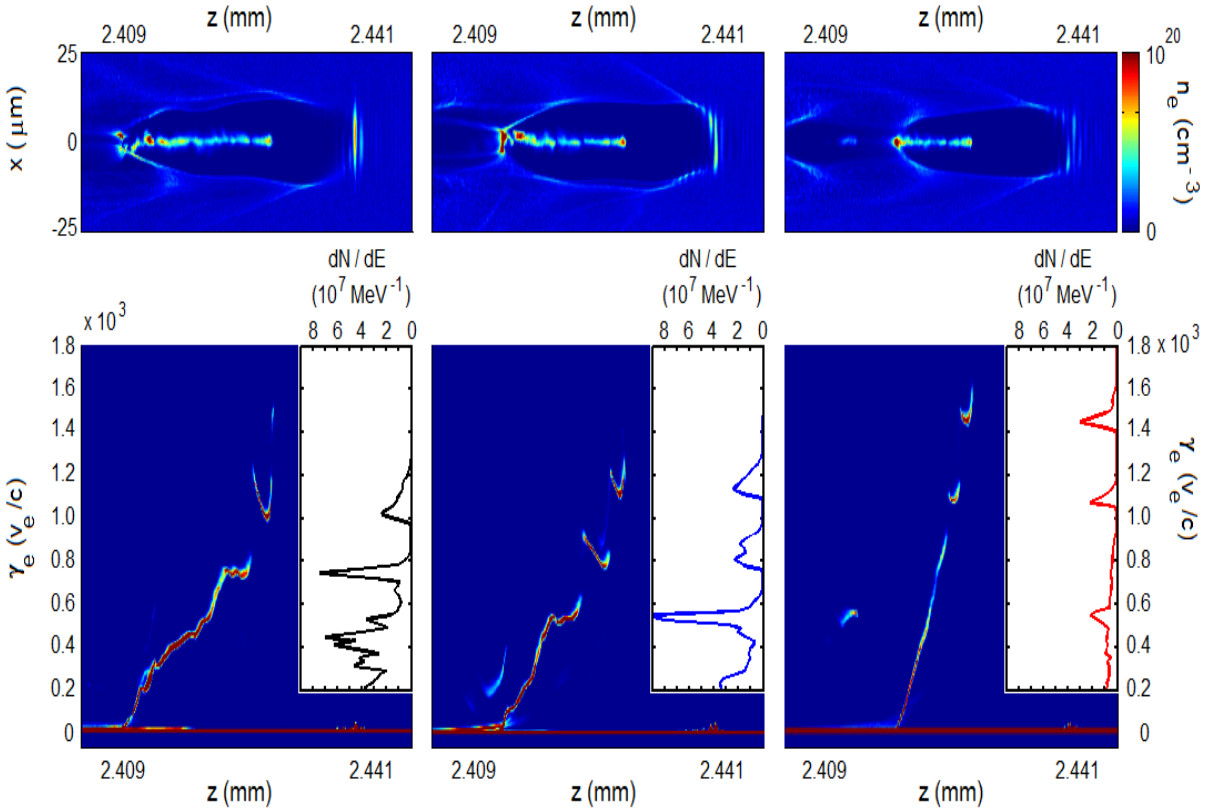

Figure 15: Producing clean comb-like electron beams in a leaky plasma channel (3D PIC simulations using CALDER-Circ code) [CP4]. Drive pulse propagates to the right. Top: snapshots of electron density. Bottom: longitudinal phase space. Left column: acceleration through dephasing in the reference case (transform-limited, 30 fs, 70 TW pulse; the plasma is uniform). Continuous elongation of the bubble causes massive continuous injection. The high-charge tail dominates the energy spectrum (see the inset). Center: acceleration through dephasing with the transform-limited pulse in the channel. The channel suppresses pulse head diffraction, reducing expansion of the bubble, and brings about periodic self-injection producing a pair of distinct QME bunches. The energy tail, however, remains as bright as in the uniform plasma. Right column: acceleration with the negatively chirped pulse (bandwidth equivalent to the 5 fs transform-limited duration) in a channel. Dispersion compensation prevents the pulse self-steepening. Combination of the chirp and the channel reduces the bubble expansion nearly by half, taking down the energy tail, producing a clean comb-like beam (see the inset). The highest-energy electrons receive ≈ 50% energy boost against the reference case, reaching 750 MeV energy over 1.8 mm acceleration distance.

ROS formation can be further delayed by using a plasma channel to suppress diffraction of the pulse leading edge, minimizing longitudinal variations in the pulse. At the same time, the combination of a bubble (a self-consistently maintained, "soft" hollow channel) and a preformed wide channel forces transverse flapping of the laser pulse tail, causing oscillations of the bubble size. The resulting periodic injection produces a polychromatic (comb-like) beam that consists of a number of background-free quasi-monoenergetic components. It is shown that periodic self-injection and acceleration transfers up to 10 percents of the drive pulse energy to several 100-pC charge, GeV-scale-energy electron bunches, each having a few-percent energy spread and ~ 1 mm mrad normalized transverse emittance. The number of these components, their charge, energy, and

energy difference can be controlled by changing the channel radius and acceleration distance, whereas negative chirp of the driver suppresses the background and boosts their energy. Such clean comb-like beams can be an asset for tunable gamma-ray table-top sources.

Production of multi-hundred-MeV electrons in sub-millimeter length plasmas: application of plasma dispersion control to the LPA experiments with ultra-broad bandwidth lasers.

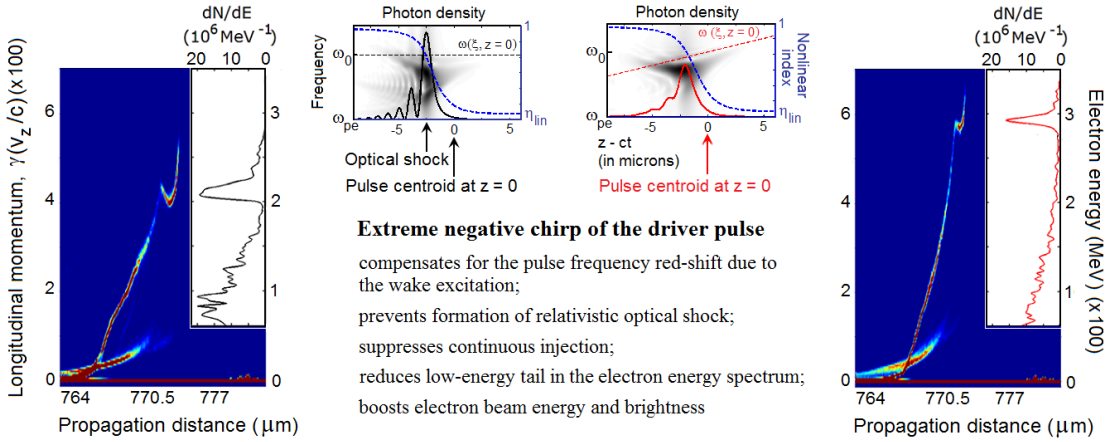

Figure 16: Laser parameters for an ultrabroadband source. Average background electron density $n_0 = 1.3 \times 10^{19}$ cm^{-3}. Phase space snapshots and energy spectra are taken after electron acceleration over 0.6 mm distance (close to dephasing limit). Left: the reference case (15 TW, 20 fs, transform limited pulse; uniform plasma). Right: acceleration in the tapered plasma (density variation ±12% of n_0 along the pulse path.) The pulse has same energy and duration, but also large bandwidth (equivalent to the 5 fs transform-limited duration) and is negatively chirped.

Compensating plasma dispersion with a negative chirp of the drive pulse, in order to prevent the build-up of the optical shock, requires the pulse frequency bandwidth of the order of the carrier frequency. We have shown that with the anticipated ultrabroadband parameters that will be available, they are well suited to the goal of background-free acceleration of electrons to hundreds of MeV relying almost entirely on the manipulations of the laser phase. The 15 TW, 20 fs pulse having the frequency bandwidth equivalent to the 5 fs transform-limited duration, when matched to self-guiding at the entrance of the plasma, produces 200-300 MeV electron bunches with a normalized transverse emittance < π mm mrad , sub-10% relative energy spread, 35-50 pC charge, and negligible low-energy background. Increasing plasma density in the pulse propagation direction (±12% of the density at the center of the target) locks electrons in the accelerating phase, boosting their energy and the beam brightness. In comparison with the reference case (20 fs transform-limited pulse in a uniform plasma), combination of the chirp and taper reduce the electron bunch charge nearly twice, increase the energy gain by ~50%, and more than double the brightness, accelerating electrons through dephasing without accumulation of the tail. This significant improvement of the beam quality is well suited for proof-of-principle experiments. As a result of this work, we conclude that investment into new pulse amplification techniques allowing for ultrahigh bandwidth (approaching the carrier wavelength) is as important for the design of future compact, high-repetition-rate, GeV-scale LPAs as investments into the approaches increasing the laser pulse energy without increase of the bandwidth.

5. Conclusion

Over the three-year project period, we made substantial progress in understanding the control of high-power light pulses, as well as their interactions and propagation at high-intensity levels. Experiments performed with both the 100-TW and 1-PW beamlines of the DIOCLES laser system have demonstrated an unprecedented level of control of high-power, ultrashort laser pulses in both the spectral and spatial domains. This has led to development of a state-of-the-art laser-driven wakefield electron accelerator, which is both tunable and controllable. This novel accelerator was in turn applied to the development of a breakthrough x-ray source based on inverse Compton scattering. In addition to being high brightness and high energy, this x-ray source is also tunable (50 keV – 10 MeV) and controllable. It is currently being applied to a number of challenging problems, such as high-resolution radiography, imaging through dense shielding, and table-top nuclear physics. Our detailed experimental, numerical and analytical studies have enabled better understanding of the physical principles underlying the interaction of these laser pulses with matter. The capabilities developed through this project have positioned the Extreme Light Laboratory at the University of Nebraska, Lincoln to continue its rapid progress in advancing high-field and ultrafast science.

6. References

[1] C. Liu, S. Banerjee, J. Zhang, S. Chen, K. Brown, J. Mills, N. Powers, B. Zhao, G. Golovin, I. Ghebregziabher, *et al*, Proc. SPIE 8599, Solid State Lasers XXII: Technology and Devices, 859919 (2013).

[2] D. Strickland and G. Mourou, Opt. Commun. **56**, 219 (1985).

[3] Z. Wang, C. Liu, Z. Shen, Q. Zhang, H. Teng, and Z. Wei, Opt. Lett. **36**, 3194 (2011).

[4] V. Malka, Phys Plasmas **19**, 055501 (2012).

[5] F. Verluise, V. Laude, Z. Cheng, C. Spielmann, and P. Tournois, Opt. Lett. **25**, 575 (2000).

[6] C. Liu, J. Zhang, S. Chen, G. Golovin, S. Banerjee, B. Zhao, N. Powers, I. Ghebregziabher, and D. Umstadter, Opt. Lett. **39**, 80 (2014).

[7] S. Y. Kalmykov, S. A. Yi, A. Beck, A. F. Lifschitz, X. Davoine, E. Lefebvre, A. Pukhov, V. Khudik, G. Shvets, S. A. Reed, *et al*, New J. Phys. **12** (2010).

[8] S. P. D. Mangles, C. D. Murphy, Z. Najmudin, A. G. R. Thomas, J. L. Collier, A. E. Dangor, E. J. Divall, P. S. Foster, J. G. Gallacher, C. J. Hooker, *et al*, Nature **431**, 535 (2004).

[9] J. Faure, Y. Glinec, A. Pukhov, S. Kiselev, S. Gordienko, E. Lefebvre, J. P. Rousseau, F. Burgy, and V. Malka, Nature **431**, 541 (2004).

[10] C. G. R. Geddes, C. Toth, J. van Tilborg, E. Esarey, C. B. Schroeder, D. Bruhwiler, C. Nieter, J. Cary, and W. P. Leemans, Nature **431**, 538 (2004).

[11] S. Y. Kalmykov, S. A. Yi, A. Beck, A. F. Lifschitz, X. Davoine, E. Lefebvre, V. Khudik, G. Shvets, and M. C. Downer, Plasma Phys. Control. Fusion **53** (2011).

[12] W. P. Leemans, B. Nagler, A. J. Gonsalves, C. Toth, K. Nakamura, C. G. R. Geddes, E. Esarey, C. B. Schroeder, and S. M. Hooker, Nat. Phys. **2**, 696 (2006).

[13] S. M. Hooker, E. Brunetti, E. Esarey, J. G. Gallacher, C. G. R. Geddes, A. J. Gonsalves, D. A. Jaroszynski, C. Kamperidis, S. Kneip, K. Krushelnick, *et al*, Plasma Physics and Controlled Fusion **49**, B403 (2007).

[14] S. Banerjee, S. Y. Kalmykov, N. D. Powers, G. Golovin, V. Ramanathan, N. J. Cunningham, K. J. Brown, S. Chen, I. Ghebregziabher, B. A. Shadwick, *et al*, Phys.Rev.ST Accel.Beams **16**, 031302 (2013).

[15] Banerjee,S., Powers, N., Ramanathan, V., Shadwick, B., Umstadter,D., Proceedings of PAC09, Particle Accelerator Conference 2009 **A14 Advance Concepts,** (2009).

[16] C. Clayton, J. Ralph, F. Albert, R. Fonseca, S. Glenzer, C. Joshi, W. Lu, K. Marsh, S. Martins, W. Mori, *et al*, Physical Review Letters **105** (2010).

[17] B. B. Pollock, C. E. Clayton, J. E. Ralph, F. Albert, A. Davidson, L. Divol, C. Filip, S. H. Glenzer, K. Herpoldt, W. Lu, *et al*, Phys. Rev. Lett. **107**, 045001 (2011).

[18] C. McGuffey, A. G. R. Thomas, W. Schumaker, T. Matsuoka, V. Chvykov, F. J. Dollar, G. Kalintchenko, V. Yanovsky, A. Maksimchuk, K. Krushelnick, *et al*, Phys. Rev. Lett. **104**, 025004 (2010).

[19] W. Lu, M. Tzoufras, C. Joshi, F. S. Tsung, W. B. Mori, J. Vieira, R. A. Fonseca, and L. O. Silva, Phys. Rev. Spec. Top. -Accel. Beams **10** (2007).

[20] V. B. Pathak, J. Vieira, R. A. Fonseca, and L. O. Silva, New Journal of Physics **14**, 023057 (2012).

[21] H. Schwoerer, B. Liesfeld, H. P. Schlenvoigt, K. U. Amthor, and R. Sauerbrey, Phys. Rev. Lett. **96**, 014802 (2006).

[22] F. Albert, S. G. Anderson, G. A. Anderson, S. M. Betts, D. J. Gibson, C. A. Hagmann, J. Hall, M. S. Johnson, M. J. Messerly, V. A. Semenov, *et al*, Optics Letters **35**, 354 (2010).

[23] E. Esarey, C. B. Schroeder, and W. P. Leemans, Rev. Mod. Phys. **81**, 1229 (2009).

[24] F. V. Hartemann, Nuclear Instruments & Methods in Physics Research Section A-Accelerators Spectrometers Detectors and Associated Equipment **608**, S1 (2009).

[25] S. Chen, N. D. Powers, I. Ghebregziabher, C. M. Maharjan, C. Liu, G. Golovin, S. Banerjee, J. Zhang, N. Cunningham, A. Moorti, *et al*, Phys. Rev. Lett. **110**, 155003 (2013).

[26] S. Kneip, C. McGuffey, J. L. Martins, S. F. Martins, C. Bellei, V. Chvykov, F. Dollar, R. Fonseca, C. Huntington, G. Kalintchenko, *et al*, Nature Physics **7**, 737 (2011).

[27] K. Ta Phuoc, S. Corde, C. Thaury, V. Malka, A. Tafzi, J. P. Goddet, R. C. Shah, S. Sebban, and A. Rousse, Nature Photonics **6**, 308 (2012).

[28] P. A. Ross, J. Opt. Soc. Am. **16**, 433 (1928).

[29] N. D. Powers, I. Ghebregziabher, G. Golovin, C. Liu, S. Chen, S. Banerjee, J. Zhang, and D. P. Umstadter, Nature Photonics **8**, 29 (2014).

[30] C. Liu, G. Golovin, S. Chen, J. Zhang, B. Zhao, D. Haden, S. Banerjee, J. Silano, H. Karwowski, and D. Umstadter, Opt. Lett. **39**, 4132 (2014).

7. Products of research activities

7.1 Publications

1. Cheng Liu, Grigory Golovin, Shouyuan Chen, Jun Zhang, Baozhen Zhao, Daniel Haden, Sudeep Banerjee, Jack Silano, Hugon Karwowski, and Donald Umstadter, "Generation of 9 MeV γ-rays by all-laser-driven Compton scattering with second-harmonic laser light," *Optics Letters* **39**, 14, 4132-4135 (2014). http://dx.doi.org/10.1364/OL.39.004132
2. Cheng Liu, Jun Zhang, Shouyuan Chen, Gregory Golovin, Sudeep Banerjee, Baozhen Zhao, Nathan Powers, Isaac Ghebregziabher, and Donald Umstadter, "Adaptive-feedback spectral-phase control for interactions with transform-limited ultrashort high-power laser pulses," *Optics Letters* **39**, 1, 80-83 (2014). http://dx.doi.org/10.1364/OL.39.000080
3. N. D. Powers, I. Ghebregziabher, G. Golovin, C. Liu, S. Chen, S. Banerjee, J. Zhang, and D. P. Umstadter, "Quasi-monoenergetic and tunable X-rays from a laser-driven Compton light source," Nature Photonics **8** 28-31 (2014). doi:10.1038/nphoton.2013.314.
4. S. Y. Kalmykov, X. Davoine, and B. A. Shadwick, "All-optical control of electron self-injection in millimeter-scale, tapered dense plasmas," *Nucl. Instrum. Methods in Phys. Res. A* **740** 266-272 (2014). http://dx.doi.org/10.1016/j.nima.2013.11.058
5. A. Beck, S. Y. Kalmykov, X. Davoine, A. Lifschitz, B. A. Shadwick, V. Malka, and A. Specka, "Physical processes at work in sub-30 fs, PW laser pulse-driven plasma accelerators: towards GeV electron acceleration experiments at CILEX facility," *Nucl. Instrum. Methods in Phys. Res. A* **740** 67-73 (2014).
6. S. Chen, N. D. Powers, I. Ghebregziabher, C. M. Maharjan, C. Liu, G. Golovin, S. Banerjee, J. Zhang, N. Cunningham, A. Moorti, S. Clarke, S. Pozzi, and D. P. Umstadter, "MeV-energy x rays from inverse Compton scattering with laser-wakefield accelerated electrons," *Phys. Rev. Lett*. **110** 15, 155003 (2013).
7. S. Banerjee, S. Y. Kalmykov, N. D. Powers, G. Golovin, V. Ramanathan, N. J. Cunningham, K. J. Brown, S. Chen, I. Ghebregziabher, B. A. Shadwick, D. P. Umstadter, B. M. Cowan, D. L. Bruhwiler, A. Beck, and E. Lefebvre, "Stable, tunable, quasimonoenergetic electron beams produced in a laser wakefield near the threshold for self-injection," *Phys. Rev. ST Accel. Beams* **16**, 031302 (2013).
8. I. Ghebregziabher, B. A. Shadwick, and D. Umstadter, "Spectral bandwidth reduction of Thomson scattered light by pulse chirping," *Phys. Rev. ST Accel. Beams* **16**, 030705 (2013).
9. B. M. Cowan, S. Y. Kalmykov, A. Beck, X. Davoine, K. Bunckers, A. F. Lifshitz, E. Lefebvre, D. L. Bruhwiler, B. A. Shadwick, and D. P. Umstadter, "Computationally efficient methods for modelling laser wakefield acceleration in the blowout regime," *J. Plasma Phys*. **78**, 469 (2012), doi: 10.1017/S0022377812000517.
10. S. Banerjee, N. D. Powers, V. Ramanathan, I. Ghebregziabher, K.J. Brown, C. M. Maharjan, S. Chen, A. Beck, E. Lefebvre, S. Y.Kalmykov, B. A. Shadwick, and D. P. Umstadter, "Generation of tunable, 100–800 MeV quasi-monoenergetic electron beams from a laser-wakefield accelerator in the blowout regime," *Phys. Plasmas* **19**, 056703 (2012).

7.2 Conference Proceedings

1. C. Liu, J. Zhang, G. Golovin, S. Chen, S. Banerjee, B. Zhao, N. Powers, I. Ghebregziabher, and D. P. Umstadter, "Adaptive spectral-phase control for laser wakefield electron acceleration," Lasers and Electro-Optics (CLEO), San Jose, CA (2014).

2. G. Golovin, S. Chen, N. Powers, C. Liu, S. Banerjee, J. Zhang, M. Zeng, Z. Sheng, and D. Umstadter, "Tunable Monoenergetic Electron Beams from Staged Ionization Assisted Laser Wakefield Accelerator," Lasers and Electro-Optics (CLEO), San Jose, CA (2014).
3. N. Powers, I. Ghebregziabher, G. Golovin, C. Liu, S. Chen, S. Banerjee, J. Zhang, and D. Umstadter, "Quasi Monoenergetic and Tunable X-rays by Laser Compton Scattering from Laser Wakefield e-beam," Lasers and Electro-Optics (CLEO), San Jose, CA (2014).
4. J. Silano, H. J. Karwowski, S. Banerjee, D. Haden, G. Golovin, S. Chen, I. Ghebregziabher, C. Liu, C. Petersen, J. Zhang, N. Powers, B. Zhao, K. Brown, J. Mills, D. Umstadter, S. Clarke, and S. Pozzi, "Selective activation with all-laser-driven Thomson γ-rays," 2013 IEEE Conference on Technologies for Homeland Security, Boston MA.
5. C. Liu, **S**. Banerjee, J. Zhang, S. Chen, K. Brown, J. Mills, N. Powers, B. Zhao, G. Golovin, I. Ghebregziabher, and D. Umstadter, "Repetitive petawatt-class laser with near-diffraction-limited focal spot and transform-limited pulse duration," Proc. SPIE **8599**, Solid State Lasers XXII: Technology and Devices, 859919 (2013).
6. S. Banerjee, J. Silano, G. Golovin, D. Haden, C. Liu, S. Chen, J. Zhang, I. Ghebregziabher, N. Powers, C. Petersen, K. Brown, J. Mills, B. Zhao, S. Clarke, S. Pozzi, H. Karwowski, and D. Umstadter, "Photodisintegration studies of actinides with laser-driven x-rays," Bulletin of the American Physical Society, Annual Meeting of the Division of Nuclear Physics **58** (2013).
7. S. Banerjee, G. Golovin, N. Powers, C.Liu, S. Chen, C. Petersen, J. Zhang, I. Ghebregziabher, B. Zhao, K. Brown, J. Mills, D. Umstadter, D. Haden, J. Silano, and H. Karwowdki, "Selective photo-activation analysis with laser-driven x-rays," Bulletin of the American Physical Society, APS April Meeting, **58** (2013).
8. S. Y. Kalmykov, "Dark-current-free laser-plasma acceleration in blowout regime using nonlinear plasma lens," AIP Conf. Proc. **1507**, 921-926 (2013). http://dx.doi.org/10.1063/1.4788989
9. S. Y. Kalmykov, B. A. Shadwick, and X. Davoine, "All-optical control of electron trapping in plasma channels," in 2013 19th IEEE Pulsed Power Conference (PPC), 1-6 (2013); ISSN: 2158-4915; ISBN 978-1-4673-5168-3. DOI: 10.1109/PPC.2013.6627518
10. B. M. Cowan, S. Y. Kalmykov, B. A. Shadwick, K. Bunkers, D. L. Bruhwiler, and D. P. Umstadter, "Improved particle statistics for laser-plasma self-injection simulations," AIP Conf. Proc. **1507**, 375-380 (2012). http://dx.doi.org/10.1063/1.4773725
11. N. Powers, S. Chen, I. Ghebregziabher, C. Maharjan, C. Liu, G. Golovin, S. Banerjee, J. Zhang, N. Cunningham, A. Moorti, S. Clarke, S. Pozzi, and D. Umstadter, "Characterization of wakefield accelerated electron beams by a spatial cross-correlation technique," in Frontiers in Optics Conference, OSA Technical Digest (online) (Optical Society of America, 2012), paper FTh1B.5. (2012).
12. I. Ghebregziabher, S. Chen, N. Powers, C. Maharjan, C. Liu, G. Golovin, S. Banerjee, J. Zhang, N. Cunningham, A. Moorti, S. Clarke, S. Pozzi, and D. Umstadter, "Bright gamma-ray beam source based on laser wakefield accelerator and laser undulator," in Frontiers in Optics Conference, OSA Technical Digest (online) (Optical Society of America, 2012), paper FTh1B.3 (2012).
13. G. Golovin, E. Grace, S. Banerjee, C. Petersen, K. Brown, J. Mills, S. Chen, C. Liu, and D. Umstadter, "Density characterization of tapered super-sonic gas jet targets for laser wakefield acceleration," American Physical Society, 54th Annual Meeting of the APS Division of Plasma Physics, October 29-November 2, abstract #UO6.014 (2012).

14. D. Umstadter, "Gigavolt-Energy Electrons and Femtosecond-Duration Hard X-Rays Driven by Extreme Light," American Physical Society, 43rd Annual Meeting of the APS Division of Atomic, Molecular and Optical Physics, June 4-8, abstract #B4.001 (2012).
15. N. Powers, S. Chen, I. Ghebregziabher, C. Maharjan, C. Liu, G. Golovin, S. Banerjee, J. Zhang, N. Cunningham, A. and Moorti, "Characterization of the source size and transverse emittance of a laser wakefield accelerated electron beam," American Physical Society, 54th Annual Meeting of the APS Division of Plasma Physics, October 29-November 2, abstract #UO6.005 (2012).
16. D. Umstadter, "Bright MeV-energy x-ray beams from a compact all-laser-driven inverse-Compton-scattering source," American Physical Society, 54th Annual Meeting of the APS Division of Plasma Physics, October 29-November 2, abstract #CI2.006 (2012).
17. S. Y. Kalmykov, X. Davoine, and B. A. Shadwick, "Sub-millimeter-scale, 100-MeV-class quasi-monoenergetic laser plasma accelerator based on all-optical control of dark current in the blowout regime," AIP Conf. Proc. **1507**, 289-294 (2012). http://dx.doi.org/10.1063/1.4773709
18. Banerjee, S., Kalmykov, S., Powers, N., Ramanathan, V., Smith, N. C., Brown, K., Chen, S., Moorthi, A., Ghebregziabher, I., Maharjan, C., Shadwick, B., Umstadter, D., Beck, A., Lefebvre, E., Cowan, A., and Bruhwiler, D., "Background-Free, Quasi-Monoenergetic Electron Beams from a Self-Injected Laser Wakefield Accelerator," Conference on Lasers and Electro-Optics/Pacific Rim, C1094, Optical Society of America (2011).
19. Bunkers, K., Kalmykov, S., Shadwick, B., Umstadter, D., Beck, A., Lefebvre, E., Cowan, B., and Bruhwiler, D., "Modeling GeV-class single-stage laser-plasma electron acceleration in the blowout regime," American Physical Society, 53rd Annual Meeting of the APS Division of Plasma Physics, November 14-18, abstract #BP9.121 (2011).\

7.3 Presentations

1. D. Umstadter, "Low-dose radiographic system: based on a novel, narrowband, tunable, multi-MeV X-ray source." Invited presentation, DNDO ARI Meeting, Leesburg, VA (June 23-25, 2014).
2. D. Umstadter, "High field electron-photon scattering." 2014 Gordon Conference on Multiphoton Processes, Boston, MA (June 15-20, 2014).
3. Cheng Liu, "Adaptive spectral-phase control for laser wakefield electron acceleration." Invited contributed talk, Laser-driven sources of particle and X-ray beams symposium, Conference on Lasers and Electro-Optics (CLEO), San Jose, CA (June 8-13, 2014).
4. Nathan D. Powers, "Quasi monoenergetic and tunable x-rays by laser compton scattering from laser wakefield e-beam." Invited contributed talk, Laser-driven sources of particle and X-ray beams symposium Conference on Lasers and Electro-Optics (CLEO), San Jose, CA (June 8-13, 2014).
5. Grigory Golovin, "Tunable monoenergetic electron beams from staged ionization assisted laser wakefield accelerator." Contributed talk, Laser-driven sources of particle and X-ray beams symposium Conference on Lasers and Electro-Optics (CLEO), San Jose, CA (June 8-13, 2014).
6. Sudeep Banerjee, "Narrowband and tunable all-laser-driven inverse-Compton x-ray source." Invited presentation, Conference on Application of Accelerators in Research and Industry (CAARI), San Antonio, TX (May 25-30, 2014).

7. Grigory Golovin, "Laser-wakefield electron accelerator with independent beam-parameter control." International Conference on Plasma Science and the International Conference on High-Power Particle Beams (ICOPS/BEAMS), Washington, D.C. (May 25-29, 2014).
8. D. Umstadter, "Experimental demonstration of a tunable and compact all-laser-driven Compton gamma-ray source." Monoenergetic Photo Source Workshop, Washington, D.C. (March 19, 2014).
9. D. Umstadter, "All-Laser-Driven Compton X-Ray Light Source," Stanford Photonics Research Center 2013 Annual Symposium, Palo Alto, California, September 16-18, 2013.
10. D. Umstadter, "Laser based acceleration today and tomorrow," 3rd International Center for Zetta- Exawatt Science and Technology Meeting, Lawrence Livermore National Laboratory, Livermore, CA, July 17-18, 2013.
11. D. Umstadter, "Laser-Produced X-Ray Sources Atomic," Molecular and Optical Science 2013 Research Meeting, Potomac, Maryland, October 27-30, 2013.
12. D. Umstadter, "A novel source for creating and probing extreme matter: femtosecond pulses of ultra-intense laser light, electrons, and gamma-rays," 1st Workshop on Materials in Extreme Environments – MatX," Michigan State University, May 13-17, 2013.
13. S. Banerjee, "Recent results from the University of Nebraska: Laser-accelerated electrons and Thomson x-rays," Laser Plasma Accelerator Workshop, Goa, India (September, 2013).
14. D. Umstadter, "Bright MeV-energy x-ray beams from a compact all-laser-driven inverse-Compton-scattering source", 54th Annual Meeting of the APS Division of Plasma Physics, Providence, RI, October 29–November 2, 2012.
15. D. Umstadter, "Research and Development with Extreme Light," National Strategic Research Institute Executive Steering Council, University of Nebraska, Lincoln, March 13, 2013.
16. D. Umstadter, "Diocles laser system: Extreme-light at high-repetition-rate," 15th Advanced Accelerator Concepts Workshop, Austin, TX, June 10-15, 2012.
17. S. Chen, "All optical driven bright Gamma ray source generated by inverse Compton scattering. 15th Advanced Accelerator Concept Workshop, Austin, TX, June 10-15, 2012.
18. D. Umstadter, "Gigavolt Energy Electrons and Femtosecond Duration Hard X-Rays Driven by Extreme Light," 43rd Annual Meeting of the APS Division of Atomic, Molecular and Optical Physics, Anaheim, CA, June 4–8, 2012.
19. D. Umstadter, "All-laser-driven x-ray synchrotron light source", Colloquium at Fermi National Accelerator Laboratory, Batavia, IL, April 11, 2012.
20. S. Chen, "Compton gamma-ray source driven by laser accelerator and undulator," Workshop on Super Intense Laser-Atomic Physics 2012, Suzhou City, China.
21. D. Umstadter, "Extreme light for probing matter from the atomic to the nuclear scale" Air Force Office of Scientific Research (AFOSR) AMO Program Review, Washington D.C., Jan. 5-6, 2012.
22. S. Banerjee, "Generation, and applications of stable, 100-500 MeV, dark-current free beams, from a laser wakefield accelerator, "Annual Meeting, Division of Plasma Physics, American Physical Society, Salt Lake City, UT (November, 2011).
23. D. Umstadter, "Propagation and Interactions of Ultrahigh Power Light: Relativistic Nonlinear Optics" Air Force Office of Scientific Research (AFOSR) AMO Program Review, Potomac, VA, Dec. 18-19, 2011.